Relation between Z3 symmetry and sign problem and analyses of pure SU(2) gauge theory based on gradient flow

開田, 丈寛

https://doi.org/10.15017/4059986

出版情報：九州大学, 2019, 博士（理学）, 課程博士
バージョン：
権利関係：

Relation between $\mathbb{Z}_3$ symmetry and sign problem and analyses of pure SU(2) gauge theory based on gradient flow

Takehiro Hirakida

Theoretical Nuclear Physics, Department of Physics
Graduate School of Science, Kyushu University
744, Motooka, Nishi-ku, Fukuoka 819-0395, Japan

Abstract

Quantum chromodynamics (QCD) describes the dynamics of quarks and gluons, and the QCD states depend on temperature and the quark chemical potential. In the low temperature and the small quark chemical potential region, quarks are confined in hadrons. In the high temperature region, quarks and gluons are in the quark-gluon plasma phase. In the low temperature and the large quark chemical potential region, it is considered that there is the color superconductor phase.

One of methods to investigate QCD states is lattice QCD. By using the theory, we can treat non-perturbative properties of QCD, and in fact many calculations have been made in both the zero and the finite temperature regions. On the other hand, in the finite quark chemical potential region, it is too difficult to obtain reliable results due to a numerical problem called the sign problem. In this thesis, in order to investigate properties of QCD in the finite quark chemical potential region, we focus on two approaches: $\mathbb{Z}_3$-QCD and 2-color QCD.

1. $\mathbb{Z}_3$ symmetry and sign problem
   The QCD-like model with exact $\mathbb{Z}_3$ symmetry is called $\mathbb{Z}_3$-QCD. It is known that $\mathbb{Z}_3$-QCD agrees with the ordinary QCD in the zero temperature limit, and numerical simulations with the spin model indicate that the sign problem of $\mathbb{Z}_3$-QCD becomes much milder than QCD. Thus, investigating $\mathbb{Z}_3$-QCD gives hints for QCD properties in the zero temperature and the finite quark chemical potential region. In this thesis, we use the effective Polyakov-line model as an effective model of lattice QCD, and discuss the relation between $\mathbb{Z}_3$ symmetry and the sign problem. The numerical results by using the reweighting method show that the region where the sign problem occurs is narrower in the $\mathbb{Z}_3$ symmetric model than that in the model corresponding to the ordinary QCD. We also improve the reweighting method, and this makes the sign problem less serious in the effective model.

2. Analyses of pure SU(2) gauge theory
   The sign problem is absent in 2-color QCD, so that it is possible to make numerical calculations in the finite quark chemical potential region. Therefore, we can check the validity of effective models by comparing both model and lattice results. When constructing an effective

model, we need thermodynamic quantities of pure SU(2) and SU(3) gauge theories. The thermodynamic quantities also have an important role to know properties of both 2-color and 3-color QCD. Recently, the gradient flow method to measure the thermodynamic quantities via the energy-momentum tensor was developed. In this thesis, we use this method to study the thermodynamics for pure SU(2) gauge theory. We determine the scale-setting function precisely, and measure thermodynamic quantities through the energy-momentum tensor. Our results are consistent with data obtained by the other methods in the high temperature region. By comparing our results with the results of pure SU($N_c \geq 3$) gauge theory, we confirm that our results have different behavior due to the difference of the order of the phase transition.

This thesis is based on the following published papers:

- Sign problem in a Z_3-symmetric effective Polyakov-line model
  T. Hirakida, J. Sugano, H. Kouno, J. Takahashi, and M. Yahiro,
  Phys. Rev. D 96, 074031 (2017).

- Thermodynamics for pure SU(2) gauge theory using gradient flow
  T. Hirakida, E. Itou, and H. Kouno,
  Prog. Theor. Exp. Phys. 2019, 033B01.

Contents

List of Figures

List of Tables

Chapter 1

Introduction

1.1 Quantum chromodynamics

The interaction between quarks and gluons is called strong interaction, one of the four fundamental interactions. The theory describing this interaction is quantum chromodynamics (QCD). This theory is non-Abelian gauge theory with the color SU(3) group. The Lagrangian density of QCD in Euclidean spacetime is written by

$$\mathcal{L}_{\rm QCD} = \bar{q}(\gamma_\mu D_\mu + M)q + \frac{1}{2g^2}{\rm tr}_c\left[F_{\mu\nu}F_{\mu\nu}\right], \tag{1.1}$$

$$D_\mu = \partial_\mu + iA_\mu, \tag{1.2}$$

$$F_{\mu\nu} = \partial_\mu A_\nu - \partial_\nu A_\mu - i[A_\mu, A_\nu] = -i[D_\mu, D_\nu], \tag{1.3}$$

where q, $\bar{q}$, and A_μ are quark, antiquark, and gluon fields, M is the quark mass, and g is the coupling constant. In Eq. (1.1), ${\rm tr}_c$ denotes the trace of color indices. With the SU(3) generator T^a, gluon fields are written by $A_\mu = \sum_a A^a_\mu T^a$. The Lagrangian density $\mathcal{L}_{\rm QCD}$ is invariant under the following local gauge transformation:

$$q(x) \to V(x)q(x),\ \bar{q}(x) \to \bar{q}(x)V^\dagger(x), \tag{1.4}$$

$$A_\mu(x) \to V(x)A_\mu(x)V^\dagger(x) + i(\partial_\mu V(x))V^\dagger(x), \tag{1.5}$$

where $V(x) = \exp\left[i\theta^a(x)T^a\right]$ with real parameters θ^a.

So far, six quarks have been discovered: up (u, $m_{\rm u} \sim 2.3$ MeV), down (d, $m_{\rm d} \sim 4.8$ MeV), strange (s, $m_{\rm s} \sim 95$ MeV), charm (c ,$m_{\rm c} \sim 1.3$ GeV), top (t, $m_{\rm t} \sim 173$ GeV), and bottom (b, $m_{\rm b} \sim 4.2$ GeV). The typical energy scale of QCD is $\Lambda_{\rm QCD} \sim 200$ MeV. Therefore, quarks with lighter mass than $\Lambda_{\rm QCD}$ have been discussed for many years.

One of the most important properties of QCD is the asymptotic freedom. This property comes from the fact that the effective coupling constant (the running coupling α_s) becomes small in the high energy scale or at the short distance. However, the coupling gets large in the low energy scale or at the long distance. The running coupling α_s as a function of the energy scale Q

is shown in Fig. 1.1. The perturbative theory reproduces the experimental results at the high energy scale where $\alpha_s < 1$. In the low energy scale, however, the perturbative analysis is unsuitable due to the large running coupling, and the non-perturbative features appear, e.g. the spontaneous breaking of chiral symmetry and the quark confinement.

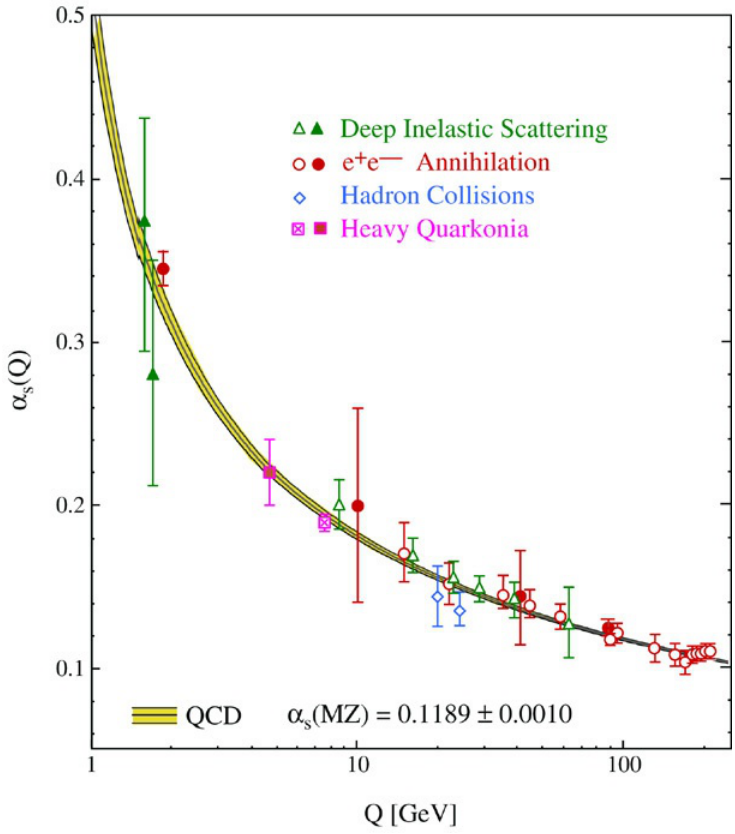

Figure 1.1: Energy-scale dependence of the running coupling constant α_s [1].

1.1.1 Spontaneous breaking of chiral symmetry

For simplicity, let us consider the quark part of 2-flavor QCD,

$$\mathcal{L}_q = \bar{q}(\gamma_\mu D_\mu + \hat{M})q, \tag{1.6}$$

where $q = (u, d)^t$, $\hat{M} = \mathrm{diag}(m_u, m_d)$. By using the chirarity operator $\gamma_5 \equiv \gamma_1\gamma_2\gamma_3\gamma_4$, we can divide quark fields q into

$$q = q_R + q_L, \quad q_{R,L} = P_{R,L}q, \quad P_R = \frac{1}{2}(1+\gamma_5), \quad P_L = \frac{1}{2}(1-\gamma_5). \tag{1.7}$$

Then, the quark part of the Lagrangian density $\mathcal{L}_q$ becomes

$$\mathcal{L}_q = \bar{q}_R\gamma_\mu D_\mu q_R + \bar{q}_L\gamma_\mu D_\mu q_L + \bar{q}_R M q_L + \bar{q}_L M q_R. \tag{1.8}$$

In the massless limit $M = 0$, the Lagrangian density is invariant under the $\mathrm{U}(2)_R \otimes \mathrm{U}(2)_L$ transformation

$$q_{R,L} \to V(\theta)_{R,L} q_{R,L}, \quad V(\theta) = \exp\left[i \sum_{a=0}^{3} \theta^a_{R,L} T^a \right], \tag{1.9}$$

where T^0 is the 2×2 unit matrix and T^i $(i = 1, 2, 3)$ is the SU(2) generator. This symmetry is called chiral symmetry. The transformation (1.9) is rewritten into $\mathrm{U}(1)_V \otimes \mathrm{U}(1)_A \otimes \mathrm{SU}(2)_V \otimes \mathrm{SU}(2)_A$. The $\mathrm{U}(1)_A$ symmetry is broken by the chiral anomaly, and the symmetry is broken into $\mathrm{U}(1)_V \otimes \mathrm{SU}(2)_V$ due to the spontaneous symmetry breaking.

The order parameter of the spontaneous breaking of chiral symmetry is the quark condensation $\langle q\bar{q} \rangle$: $\langle q\bar{q} \rangle = 0$ when chiral symmetry is preserved, and $\langle q\bar{q} \rangle \neq 0$ when the symmetry is broken spontaneously. When the symmetry is broken spontaneously, n massless bosons (NG-bosons) are generated, where n is the number of generators for the broken symmetry (Nambu-Goldstone theorem). In the case of 2-flavor QCD, the generated massless bosons are three pions $(\pi^0, \pi^\pm)$.

In 2-flavor QCD, quarks have finite but small masses. Therefore, chiral symmetry is approximately preserved, and hence NG-bosons have small masses. In the spontaneous chiral symmetry broken phase, the quark condensation $\langle q\bar{q} \rangle$ is finite, so that the nucleon masses become larger than the sum of masses of three quarks.

1.1.2 Quark confinement

The interaction between a quark and an antiquark becomes larger as the running coupling α_s increases. Thus, when α_s is large, quarks are confined in hadrons and we cannot observe quarks alone. This property is called the quark confinement, and the transition into the deconfined state is called the confinement-deconfinement transition. This transition is related to the center symmetry of QCD ($\mathbb{Z}_3$ symmetry).

In QCD, we usually take the boundary conditions for quark and gluon fields in the temporal direction as

$$q(\boldsymbol{x}, x_4 = 1/T) = -q(\boldsymbol{x}, x_4 = 0), \tag{1.10}$$

$$A_\mu(\boldsymbol{x}, x_4 = 1/T) = A_\mu(\boldsymbol{x}, x_4 = 0). \tag{1.11}$$

For the gauge transformation $V(x)$, we take the boundary condition as

$$V(\boldsymbol{x}, x_4 = 1/T) = V(\boldsymbol{x}, x_4 = 0). \tag{1.12}$$

Under the gauge transformation with Eq. (1.12), the Lagrangian density (1.1) and the boundary conditions (1.10) and (1.11) are not changed. Next,

we consider the gauge transformation with the $\mathbb{Z}_3$ transformed boundary condition:

$$V(\boldsymbol{x}, x_4 = 1/T) = e^{-i2\pi k/3} V(\boldsymbol{x}, x_4 = 0) \quad (k \in \mathbb{Z}). \tag{1.13}$$

By using this, the boundary condition for quark fields (1.10) is changed into

$$q(\boldsymbol{x}, x_4 = 1/T) = -e^{i2\pi k/3} q(\boldsymbol{x}, x_4 = 0), \tag{1.14}$$

while that for gluon fields (1.11) is invariant. Therefore, $\mathbb{Z}_3$ symmetry of QCD with quarks is explicitly broken via the boundary condition (1.10).

Now, let us consider pure SU(3) gauge theory at finite temperature. Gluon fields $A_\mu(x)$ are periodic in the temporal direction, and we can construct the following gauge-invariant operator,

$$L(\boldsymbol{x}) \equiv \frac{1}{N_c} \mathcal{T} \exp\left[i \int_0^{1/T} dx_4 \; A_\mu(\boldsymbol{x}, x_4) \right], \tag{1.15}$$

where $\mathcal{T}$ denotes the time-ordered product, and N_c represents the number of colors. This is called the Polyakov loop. Under the gauge transformation with the boundary condition (1.13), this operator is changed into

$$\Phi(\boldsymbol{x}) \equiv \mathrm{tr}_c[L(\boldsymbol{x})] \to e^{-i2\pi k/3} \Phi(\boldsymbol{x}). \tag{1.16}$$

It is known that the confinement-deconfinement transition is the first order, and $\langle \Phi \rangle$ is finite at high temperature and zero at low temperature. This quantity breaks $\mathbb{Z}_3$ symmetry, so $\langle \Phi \rangle$ is an order parameter of it.

In the infinite quark mass limit, $\langle \Phi(\boldsymbol{x}) \rangle$ is derived by

$$\langle \Phi(\boldsymbol{x}) \rangle = e^{-F_q/T}, \tag{1.17}$$

where F_q is the free energy of the static quark. When $\langle \Phi(\boldsymbol{x}) \rangle = 0$, F_q diverges. This indicates that we need the infinite energy to obtain a quark, and thus quarks are confined in hadrons. On the other hand, when F_q is finite, $\langle \Phi(\boldsymbol{x}) \rangle$ is also finite, and then we can extract a quark.

1.1.3 Phase diagram of QCD

The states of quarks and gluons depend on temperature T and the quark chemical potential μ_q. In the low T and the low μ_q region, quarks are confined in hadrons, and this phase is called the hadronic phase, where $\mathbb{Z}_3$ symmetry is weakly preserved and chiral one is weakly broken. In the high T region, quarks and gluons are in the quark-gluon plasma (QGP) phase, where they behave almost as free particles. In this phase, $\mathbb{Z}_3$ symmetry is broken and chiral symmetry is restored. In the low T and the large μ_q region, it is considered that there is the color superconductor phase, where the cooper

pairs of quarks are formed. This phase is expected to exist inside of the high density star such as a neutron star.

The schematic figure, so-called the QCD phase diagram, is shown in Fig. 1.2. This diagram is investigated by both theoretical and experimental studies, but the wide region, i.e. the finite μ_q region, is not understood completely. Thus, investigating the QCD phase diagram in the finite μ_q region is one of the most important subjects in hadron physics.

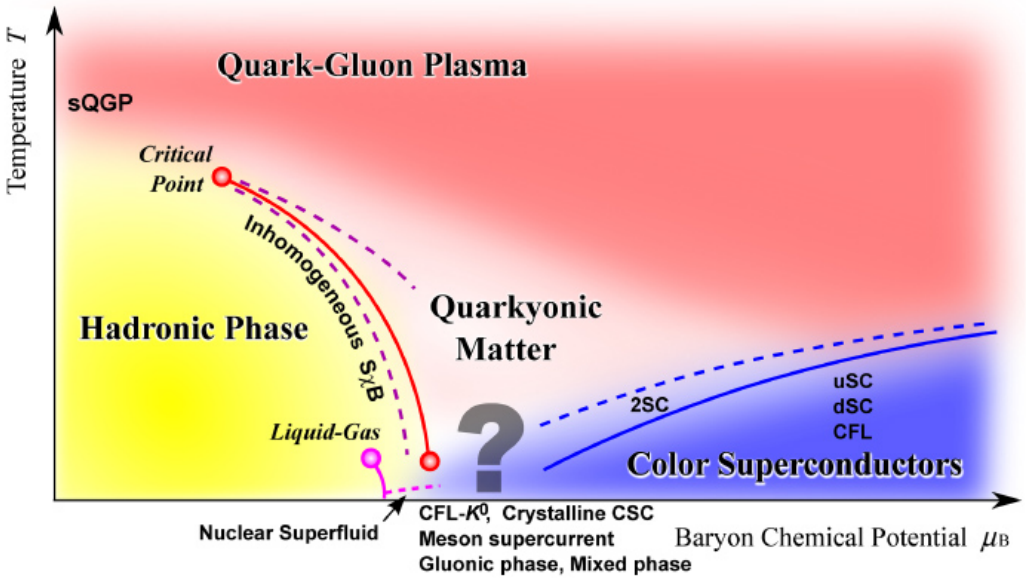

Figure 1.2: QCD phase diagram in the μ_B–T plane [2], where μ_B is the baryon chemical potential ($\mu_B = 3\mu_q$).

1.2 Lattice QCD

The lattice QCD (LQCD) simulation is one of methods to study the QCD phase diagram. LQCD is formulated in the discretized spacetime, and the partition function after integrating quark fields is given by

$$Z = \int \mathcal{D}U \ \det[\mathcal{M}(\mu_q)] \exp\left[-S_G\right], \tag{1.18}$$

$$S_G = \int d^4x \ \frac{1}{2g^2} \mathrm{tr}_c \left[F_{\mu\nu} F_{\mu\nu}\right], \tag{1.19}$$

$$\mathcal{M}(\mu_q) = \gamma_\mu D_\mu + m - \gamma_4 \mu_q, \tag{1.20}$$

where $\det[\mathcal{M}(\mu_q)]$ is the fermion determinant, and U is the link variable defined by

$$U_\mu(x) = \exp\left[iaA_\mu(x)\right], \tag{1.21}$$

where a is a lattice spacing.

In LQCD simulations, the Monte Carlo method is usually used to evaluate the integration in the partition function (1.18). Then, we treat the integrand $\rho(\mu_q) = \det[\mathcal{M}(\mu_q)]e^{-S_G}$ as a probability weight, so that $\rho(\mu_q)$ is needed to be real and positive.

1.2.1 Sign problem

The determinant $\det[\mathcal{M}(\mu_q)]$ satisfies the following relation:

$$(\det[\mathcal{M}(\mu_q)])^* = \det\left[\gamma_5\mathcal{M}(-\mu_q^*)\gamma_5\right] = \det\left[\mathcal{M}(-\mu_q^*)\right]. \tag{1.22}$$

When μ_q is zero or a pure imaginary number, the determinant becomes real. However, when μ_q is real or complex, the determinant becomes complex. Therefore, LQCD simulations based on the Monte Carlo method are much difficult. This problem is so-called the sign problem.

To avoid the sign problem, several methods are proposed and tested, e.g. the reweighting method [3], and the Taylor expansion method [4, 5]. Recent years, numerical simulations based on the Complex Langevin method [6–8] and the Lefschetz thimble method [9, 10] have progressed. However, it is still too difficult to obtain reliable results especially in the large μ_q region.

1.2.2 $\mathbb{Z}_3$-symmetric QCD-like model and sign problem

As mentioned in Sec. 1.1.2, $\mathbb{Z}_3$ symmetry in QCD with dynamical quarks breaks explicitly through the boundary condition for quark fields. For the three flavor case, instead of the ordinary boundary condition for quarks, we can restore $\mathbb{Z}_3$ symmetry by introducing the flavor-dependent twist boundary condition [11]. The QCD-like model with this condition is called $\mathbb{Z}_3$-QCD, and its properties were investigated by using an effective model such as the Polyakov-loop-extended Nambu–Jona-Lasinio (PNJL) model [11–15]. In addition, the lattice simulation of $\mathbb{Z}_3$-QCD was carried out at $\mu_q = 0$ [16], and the results were consistent with the PNJL-model predictions.

In Ref. [15], it was also predicted that the sign problem becomes milder in $\mathbb{Z}_3$-QCD than in the ordinary QCD. In order to examine this prediction, Hirakida *et al.* [17] performed a numerical simulation by using the $\mathbb{Z}_3$-symmetric 3D several-state Potts model as a toy model of $\mathbb{Z}_3$-QCD. It was confirmed that the sign problem is much milder in the $\mathbb{Z}_3$-symmetric model than in the model without exact $\mathbb{Z}_3$ symmetry. Thus, it is expected that we can perform the lattice calculation of $\mathbb{Z}_3$-QCD in the large quark chemical potential region.

1.2.3 Sign problem in 2-color QCD

In 2-color QCD, the fermion determinant satisfies the same relation shown in Eq. (1.22). In addition, the determinant also has the following relation:

$$\det[\mathcal{M}(\mu_q)] = \det[(\sigma_2 C\gamma_5)^\dagger \mathcal{M}(\mu_q)(\sigma_2 C\gamma_5)] = \det[\mathcal{M}(\mu_q^*)]^*, \tag{1.23}$$

where $C \equiv \gamma_2\gamma_4$ is the charge conjugation matrix, and σ_2 is the second Pauli matrix in the color space. Due to this relation, the fermion determinant becomes real, and it is possible to carry out lattice calculations of 2-color QCD in the real μ_q region. In fact, several calculations were done in Refs. [18–29].

Once obtaining thermodynamic quantities and the expectation value of the Polyakov loop of pure SU(2) gauge theory, it is possible to construct an effective model of 2-color QCD. In Refs. [27, 30, 31], the PNJL model for 2-color QCD was constructed and the validity of the model was tested by comparing the model and the lattice results. However, in these researches, thermodynamic quantities of pure SU(2) gauge theory are not used to determine the effective potential. Thus, these model results may not be realistic. It is needed to improve the effective Polyakov loop potential by using lattice results of pure SU(2) gauge theory.

1.2.4 Thermodynamic quantity of pure SU(N_c) gauge theory

Thermodynamic quantities have an important role to know properties of QCD. Several methods (e.g. integral method [32], moving-frame method [33]) have been proposed and used in lattice calculations of both pure SU(N_c) gauge theory and QCD with dynamical quarks. These results in pure SU(N_c) gauge theory are consistent with the prediction of the gluon gas model and the Hard-Thermal-Loop model [34] in the high temperature region, while they are well explained by the massive glueball model in the low temperature region.

Transport coefficients are also important in the finite temperature region. For intermediate temperature, experimental data show the small ratio of the shear viscosity to the entropy density η/s. This result indicates that the QCD state in that temperature is consistent with a perfect liquid rather than a gas [35]. In the theoretical side, the work in Ref. [36] shows the lower bound for η/s by using a large-N_c analysis based on AdS/CFT correspondence. However, the correction terms of $1/N_c$ have not been determined yet. In lattice calculations, methods to obtain viscosities were proposed and tested [37–40]. The first step is measuring the correlation function of the energy-momentum tensor (EMT), and there are several problems, e.g. the small signal-to-noise ratio of correlation functions [39], the definition of the

renormalization of the EMT as a conserved quantity on the lattice, and obtaining the spectral function from correlation functions.

In the lattice gauge theory, constructing the EMT on the lattice is also difficult, since the lattice regularization breaks the translational symmetry. In recent years, Suzuki proposed a new method to measure the EMT in Ref. [41] by using the gradient flow [42, 43]. When using this method, the statistical error becomes smaller than that by the other methods, and the wave function renormalization of the EMT is not needed in pure SU(N_c) gauge theory. Due to these advantages, the method based on the gradient flow was applied to pure SU(3) gauge theory [44], and the result is consistent with that obtained by other methods. Moreover, this method has been extended to QCD with dynamical quarks [45]. Therefore, by applying this method, it is expected that the results of pure SU(2) gauge theory provide the large signal for the $1/N_c$ correction terms.

1.3 Strategy

It is important to investigate the QCD phase diagram at the finite quark chemical potential μ_q. One of methods to study the QCD dynamics is LQCD simulations. However, it is difficult to carry out LQCD simulations at the finite quark chemical potential due to the sign problem. In order to avoid this problem, several applications are proposed, but it is still difficult to obtain reliable results. In this thesis, we adopt two approaches to investigate properties of QCD in the real μ_q region: $\mathbb{Z}_3$-QCD and 2-color QCD.

$\mathbb{Z}_3$-QCD agrees with the ordinary QCD in the zero temperature limit. In Ref. [17], the numerical simulation with the spin model as the QCD-like model shows that the sign problem is much milder in the $\mathbb{Z}_3$ symmetric model than in the QCD-like spin model. Therefore, it is expected that the approach with $\mathbb{Z}_3$-QCD gives hints for properties of QCD in the zero temperature and the finite μ_q region, e.g. nuclear matters and neutron stars. In this thesis, we use the effective Polyakov-line model [46] as an effective model of LQCD, and make numerical simulations based on the reweighting method in the finite μ_q region. We also improve the reweighting method and test the efficiency of it with the effective Polyakov-line model.

In lattice calculations of 2-color QCD, there is no sign problem since the fermion determinant becomes real. Therefore, we can check the validity of effective models such as the PNJL model by comparing the model results with the lattice results in the real μ_q region. To construct an effective model, thermodynamic quantities of pure SU(2) gauge theory is needed. In addition, thermodynamic quantities have an important role to understand properties of both 2-color and 3-color QCD. In order to construct the effective model of 2-color QCD and measure η/s, in this thesis, we determine the scale-setting function, which gives the relation between the lattice spacing and the

lattice coupling constant, and measure thermodynamic quantities by using the gradient flow. Several researches [32,47–49] show the numerical results of thermodynamics for pure SU(2) gauge theory without the continuum limit. Thus, we take the continuum limit of the thermodynamic data carefully, and compare with the results of other methods.

This thesis is constructed as follows. In Chap. 2, we discuss the relation between $\mathbb{Z}_3$ symmetry and the sign problem with the effective Polyakov-line model. In Chat. 3, we analyze the thermodynamics of pure SU(2) gauge theory based on the gradient flow. Finally, in Chap. 4, we summarize our results.

Chapter 2

$\mathbb{Z}_3$ symmetry and sign problem

2.1 $\mathbb{Z}_3$-QCD

Let us consider 3-flavor QCD. In QCD with dynamical quarks, $\mathbb{Z}_3$ symmetry is explicitly broken. To restore this symmetry, we first introduce the flavor-dependent twist boundary condition (FTBC) [11–15],

$$q_f(\boldsymbol{x}, x_4 = 1/T) = -e^{-i\theta_f} q_f(\boldsymbol{x}, x_4 = 0),\ \theta_f = \frac{2\pi}{3} f \quad (f = -1, 0, 1), \tag{2.1}$$

instead of the anti-periodic boundary condition (1.10). Here, the integer f represents the flavor index, for convenience. After the $\mathbb{Z}_3$ transformation shown in Eq. (1.13), the FTBC (2.1) becomes

$$\begin{aligned} q_f(\boldsymbol{x}, x_4 = 1/T) &= -e^{-i\theta_f + i2\pi k/3} q_f(\boldsymbol{x}, x_4 = 0) \\ &= -e^{-i\theta'_f} q_f(\boldsymbol{x}, x_4 = 0),\ \theta'_f = \frac{2\pi}{3}(f - k). \end{aligned} \tag{2.2}$$

By relabeling $f - k$ as f', this transformed boundary condition returns to the original one, and the boundary condition for quarks becomes invariant under the $\mathbb{Z}_3$ transformation. The demonstration of the FTBC in the case of $k = 1$ is shown in Fig. 2.1

The QCD-like theory with the boundary condition (2.1) is invariant under the $\mathbb{Z}_3$ transformation. This QCD-like theory is called $\mathbb{Z}_3$-QCD. In the zero temperature limit, $\mathbb{Z}_3$-QCD agrees with QCD because the temporal boundary condition is not relevant.

After the transformation

$$q_f \to e^{-i\theta_f T x_4} q_f, \tag{2.3}$$

the FTBC returns to the original boundary condition (1.10), and the quark part of the Lagrangian density becomes

$$\mathcal{L}_{F,\mathbb{Z}_3} = \bar{q}(\gamma_\mu D_\mu + \hat{M} - i\gamma_4 \hat{\theta} T) q, \tag{2.4}$$

where $\hat{\theta} = \mathrm{diag}\big(\theta_{-1}, \theta_0, \theta_1\big)$ refers the flavor-dependent imaginary chemical potential rescaled by temperature T. Obviously, because of the existence of

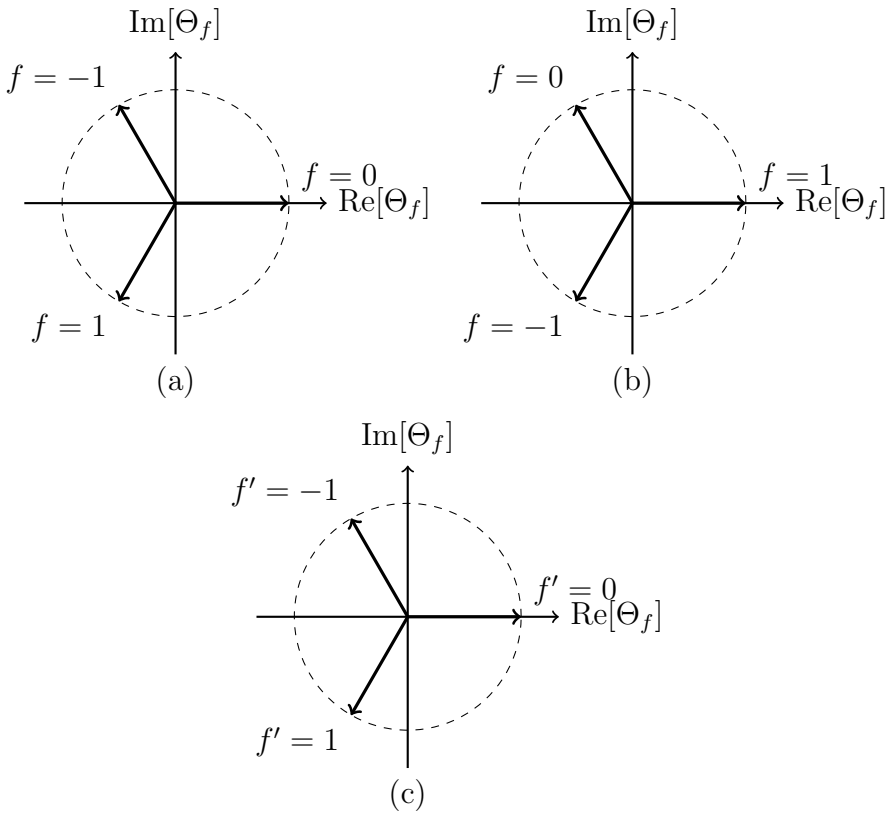

Figure 2.1: Conceptual diagram of the FTBC in the case of $k = 1$. Here, $\Theta_f \equiv e^{-i\theta_f}$. (a) The initial state. (b) The state after the $\mathbb{Z}_3$ transformation. θ_f is rotated by $2\pi/3$ in the complex plane. (c) Relabeling $f - k$ as f'. After that, the rotated state returns to the initial one.

$\hat{\theta}$, the flavor SU(3) symmetry is partially broken. In the massless limit ($\hat{M} \to 0$), global $\mathrm{SU}(3)_V \otimes \mathrm{SU}(3)_A$ symmetry is broken down to $(\mathrm{U}(1)_V)^2 \otimes (\mathrm{U}(1)_A)^2$. When the chiral symmetry is spontaneously broken, the remaining symmetry is $(\mathrm{U}(1)_V)^2$.

2.2 Effective Polyakov-line model

To study the efficiency of $\mathbb{Z}_3$-QCD in the finite quark chemical potential region, we use the effective Polyakov-line (EPL) model [46, 50, 51]. In the temporal gauge $A_4 = 0$ except for a timeslice at $x_4 = 0$, the effective action S_P for the EPL model is determined by

$$e^{-S_P} = \int \mathcal{D}U_4(\boldsymbol{x}, 0)\mathcal{D}U_i\mathcal{D}\phi \left\{ \prod_{\boldsymbol{x}} \delta[U_{\boldsymbol{x}} - U_4(\boldsymbol{x}, 0)] \right\} e^{-S_L}, \qquad (2.5)$$

where ϕ denotes the pseudofermion of boson fields, S_L is the lattice action, and $U_{\boldsymbol{x}}$ represents the Polyakov line holonomy

$$U_{\boldsymbol{x}} = \mathrm{diag}\left\{e^{i\varphi_{r,\boldsymbol{x}}}, e^{i\varphi_{g,\boldsymbol{x}}}, e^{i\varphi_{b,\boldsymbol{x}}}\right\}, \quad \sum_{i=r,g,b}^{3} \varphi_{i,\boldsymbol{x}} = 0. \tag{2.6}$$

The partition function of the EPL model is written by

$$Z = \int \mathcal{D}U \ \exp\left[-S_P[U_{\boldsymbol{x}}]\right], \tag{2.7}$$

By using Eq. (2.5), we obtain the SU(3) spin model in the three-dimensional space $V = N_s^3$ as an effective model of LQCD. In the strong coupling limit, the effective gauge action becomes [50–53]

$$S_G = -\kappa \sum_{\boldsymbol{x}} \sum_{i=1}^{3} \left\{ \mathrm{tr}\left[U_{\boldsymbol{x}}\right] \mathrm{tr}\left[U^{\dagger}_{\boldsymbol{x}+\hat{\boldsymbol{i}}}\right] + \mathrm{c.c.} \right\}, \tag{2.8}$$

where κ is the effective coupling constant. The relation between κ and temperature T is complicated like that between the lattice coupling β and T. Thus, in order to investigate the qualitative properties of the phase structures and the sign problem, we use the simple form presented in Refs. [53,54]: the large κ corresponds to high temperature, while the small one does to low temperature.

By using the relation Eq. (2.6), the dynamical variables for the EPL model are changed into $\varphi_{i,\boldsymbol{x}}$. Then, the Haar measure $\mathcal{D}U$ becomes

$$\mathcal{D}U = \mathcal{D}\varphi_r \mathcal{D}\varphi_g \ e^{-S_H}, \ S_H = \sum_{\boldsymbol{x}} L_H(\boldsymbol{x}), \tag{2.9}$$

$$L_H(\boldsymbol{x}) = -\log\left[\sin^2\left(\frac{\varphi_{r,\boldsymbol{x}} - \varphi_{g,\boldsymbol{x}}}{2}\right) \sin^2\left(\frac{2\varphi_{r,\boldsymbol{x}} + \varphi_{g,\boldsymbol{x}}}{2}\right) \times \sin^2\left(\frac{\varphi_{r,\boldsymbol{x}} + 2\varphi_{g,\boldsymbol{x}}}{2}\right)\right]. \tag{2.10}$$

For the fermion action, we consider the heavy dense and the static quark. The effective action S_F is given by [55–57]

$$\begin{aligned} S_F &= \sum_{\boldsymbol{x}} L_F(\boldsymbol{x}), \\ L_F(\boldsymbol{x}) &= -2N_f \log\left\{\det\left[1 + h_+ U_{\boldsymbol{x}}\right] \det\left[1 + h_- U^{\dagger}_{\boldsymbol{x}}\right]\right\} \\ &= -2N_f \left\{\log\left[1 + h_+ \mathrm{tr}[U_{\boldsymbol{x}}] + h_+^2 \mathrm{tr}[U^{\dagger}_{\boldsymbol{x}}] + h_+^3\right] \right. \\ &\qquad \left. + \log\left[1 + h_- \mathrm{tr}[U^{\dagger}_{\boldsymbol{x}}] + h_-^2 \mathrm{tr}[U_{\boldsymbol{x}}] + h_-^3\right]\right\} \qquad (2.11) \\ h_{\pm} &= e^{(\pm\mu - M)/T}, \qquad (2.12) \end{aligned}$$

where N_f is the number of flavors, and M, μ, and T denote the heavy quark mass, the quark chemical potential, and temperature, respectively. In the

limit $M \to \infty$, the Lagrangian density $L_F(\boldsymbol{x})$ is almost real when $\mu = M$, since $h_+ = 1$ and $h_- \to 0$ in Eq. (2.11). This property is related to the particle-hole symmetry.

From the above, the partition function of the EPL model is derived by

$$Z = \int \mathcal{D}\varphi_r \mathcal{D}\varphi_g \; e^{-S_G - S_F - S_H}, \tag{2.13}$$

and we call this EPLMWO, for simplicity. In this study, we consider the case of $N_f = 3$.

From Eq. (2.6), we can define the (traced) Polyakov line as

$$P_{\boldsymbol{x}} = \frac{1}{3}\mathrm{tr}[U_{\boldsymbol{x}}] = \frac{1}{3}\left(e^{i\varphi_{r,\boldsymbol{x}}} + e^{i\varphi_{g,\boldsymbol{x}}} + e^{i\varphi_{b,\boldsymbol{x}}}\right). \tag{2.14}$$

(In general, $P_{\boldsymbol{x}}$ is called the Polyakov loop, but in this study we call it the Polyakov line according to Ref. [46, 50, 51].) This quantity is not invariant under the $\mathbb{Z}_3$ transformation $U_{\boldsymbol{x}} \to e^{i2\pi k/3}U_{\boldsymbol{x}}$ ($k \in \mathbb{Z}$), and is an order parameter of the confinement-deconfinement transition just as the case of pure SU(3) gauge theory or QCD.

2.2.1 Particle-hole symmetry

In the large mass limit, the contribution of the second term in Eq. (2.11) can be ignored, since $h_- \to 0$ and this term becomes constant. Therefore, we now consider only the first term in Eq. (2.11). When $\mu = M + \delta\mu$, the Lagrangian density becomes

$$\begin{aligned} L_F(\boldsymbol{x})|_{\mu=M+\delta\mu,\varphi_i} &\sim -2N_F \log\left[1 + e^{\delta\mu/T}\mathrm{tr}[U_{\boldsymbol{x}}] + e^{2\delta\mu/T}\mathrm{tr}[U_{\boldsymbol{x}}^\dagger] + e^{3\delta\mu/T}\right] \\ &= -6N_F\delta\mu/T \\ &\quad - 2N_F \log\left[1 + e^{-\delta\mu/T}\mathrm{tr}[U_{\boldsymbol{x}}^\dagger] + e^{-2\delta\mu/T}\mathrm{tr}[U_{\boldsymbol{x}}] + e^{-3\delta\mu/T}\right] \\ &= -6N_F\delta\mu/T + L_F(\boldsymbol{x})|_{\mu=M-\delta\mu,-\varphi_i}. \end{aligned} \tag{2.15}$$

The first term $-6N_F\delta\mu/T$ doesn't contribute the expectation values of observables since it is independent of the dynamical variables φ_i. Thus, the relation $L_F|_{\mu=M+\delta\mu,\varphi_i} = L_F|_{\mu=M-\delta\mu,-\varphi_i}$ is effectively satisfied, and the expectation value of any quantity $\mathcal{O}$ without the explicit μ-dependence has the relation $\langle\mathcal{O}(\mu = M + \delta\mu)\rangle = \langle\mathcal{O}(\mu = M - \delta\mu)\rangle$. This relation is called the particle-hole symmetry [56]. At $\mu = M$, the Lagrangian density becomes

$$\begin{aligned} L_F(\boldsymbol{x})|_{\mu=M,\varphi_i} &\sim -2N_F \log\left[1 + \mathrm{tr}[U_{\boldsymbol{x}}] + \mathrm{tr}[U_{\boldsymbol{x}}^\dagger] + 1\right] \\ &= -2N_F \log\left[2(1 + \mathrm{Re}\{\mathrm{tr}[U_{\boldsymbol{x}}]\})\right]. \end{aligned} \tag{2.16}$$

When $(1 + \mathrm{Re}\{\mathrm{tr}[U_{\boldsymbol{x}}]\}) < 0$, the Lagrangian density (2.16) becomes complex. However, the imaginary part is an integer multiple of 2π. Thus, the sign problem does not occur at $\mu = M$.

2.2.2 $\mathbb{Z}_3$-symmetric EPL model

In EPLMWO, $\mathbb{Z}_3$ symmetry is explicitly broken since $\mathrm{tr}[U_{\boldsymbol{x}}]$ in the Lagrangian density L_F is not invariant under the $\mathbb{Z}_3$ transformation. To construct the $\mathbb{Z}_3$-symmetric EPL model, we introduce the flavor-dependent imaginary chemical potential $i\theta_f T$, $(\theta_u, \theta_d, \theta_s) = (0, 2\pi/3, -2\pi/3)$, following the manner of $\mathbb{Z}_3$-QCD. The corresponding Lagrangian density $L_{F,\mathbb{Z}_3}(\boldsymbol{x})$ is derived by

$$\begin{aligned}
L_{F,\mathbb{Z}_3}(\boldsymbol{x}) &= -2\sum_{f=u,d,s}\log\left\{\det\left[1+h_+e^{i\theta_f}U_{\boldsymbol{x}}\right]\det\left[1+h_-e^{-i\theta_f}U_{\boldsymbol{x}}^\dagger\right]\right\} \\
&= -2\log\left\{\prod_{f=u,d,s}\det\left[1+h_+e^{i\theta_f}U_{\boldsymbol{x}}\right]\det\left[1+h_-e^{-i\theta_f}U_{\boldsymbol{x}}^\dagger\right]\right\} \\
&= -2\log\left\{\det\left[1+h_+^3(U_{\boldsymbol{x}})^3\right]\det\left[1+h_-^3(U_{\boldsymbol{x}}^\dagger)^3\right]\right\} \\
&= -2\left\{\log\left[1+h_+^3\mathrm{tr}[(U_{\boldsymbol{x}})^3]+h_+^6\mathrm{tr}[(U_{\boldsymbol{x}}^\dagger)^3]+h_+^9\right]\right. \\
&\qquad\left.+\log\left[1+h_-^3\mathrm{tr}[(U_{\boldsymbol{x}}^\dagger)^3]+h_-^6\mathrm{tr}[(U_{\boldsymbol{x}})^3]+h_-^9\right]\right\}.
\end{aligned} \tag{2.17}$$

It is easily seen that $\mathrm{tr}[(U_{\boldsymbol{x}})^3]$ and $\mathrm{tr}[(U_{\boldsymbol{x}}^\dagger)^3]$ are invariant under the $\mathbb{Z}_3$ transformation, and thus the Lagrangian density $L_{F,\mathbb{Z}_3}$ has the explicit $\mathbb{Z}_3$ symmetry. As in EPLMWO, this model also has the particle-hole symmetry. Hereafter, we refer this model to $\mathbb{Z}_3$-EPLM.

For $\mathrm{tr}[(U_{\boldsymbol{x}})^3]$, the (traced) cubic Polyakov line is defined by

$$Q_{\boldsymbol{x}} = \frac{1}{3}\mathrm{tr}[(U_{\boldsymbol{x}})^3] = \frac{1}{3}\left(e^{i3\varphi_{r,\boldsymbol{x}}}+e^{i3\varphi_{g,\boldsymbol{x}}}+e^{i3\varphi_{b,\boldsymbol{x}}}\right), \tag{2.18}$$

and written with $P_{\boldsymbol{x}}$ as

$$Q_{\boldsymbol{x}} = 9\left\{(P_{\boldsymbol{x}})^3 - P_{\boldsymbol{x}}P_{\boldsymbol{x}}^*\right\}+1. \tag{2.19}$$

The cubic Polyakov line is invariant under the $\mathbb{Z}_3$ transformation, thus this is not an order parameter of the confinement-deconfinement transition. From the relation (2.19), it is easily seen that the degeneration between the confined state $P_{\boldsymbol{x}}=0$ and the deconfined ones $P_{\boldsymbol{x}}=1, e^{\pm i2\pi/3}$ occurs, since $Q_{\boldsymbol{x}}=Q_{\boldsymbol{x}}^*=1$ are in both states. Figure 2.2 shows the allowed regions of $P_{\boldsymbol{x}}$ and $Q_{\boldsymbol{x}}$ in the complex plane. In the left panel for $P_{\boldsymbol{x}}$, both states $e^{\pm i2\pi/3}$ are the $\mathbb{Z}_3$ images of the deconfined one $P_{\boldsymbol{x}}=1$.

In the complex plane of $Q_{\boldsymbol{x}}$, the point $Q_{\boldsymbol{x}}=1$ corresponds to that of $P_{\boldsymbol{x}}=0$ and $P_{\boldsymbol{x}}=1, e^{\pm i2\pi/3}$, as mentioned above. The origin $Q_{\boldsymbol{x}}=0$ corresponds to a configuration $(\varphi_{r,\boldsymbol{x}}, \varphi_{g,\boldsymbol{x}}, \varphi_{b,\boldsymbol{x}}) = (2\pi/9, -2\pi/9, 0)$ and its Weyl-symmetry transformed ones. The states $Q_{\boldsymbol{x}}=e^{\pm i2\pi/3}$, where the absolute value of $\mathrm{Im}[Q_{\boldsymbol{x}}]$ is maximum and the sign problem is the severest in $\mathbb{Z}_3$-EPLM, correspond to configurations $(\varphi_{r,\boldsymbol{x}}, \varphi_{g,\boldsymbol{x}}, \varphi_{b,\boldsymbol{x}}) = (\pm 2\pi/9, \pm 2\pi/9, \mp 4\pi/9)$ and their $\mathbb{Z}_3$ and/or Weyl-symmetry transformed ones.

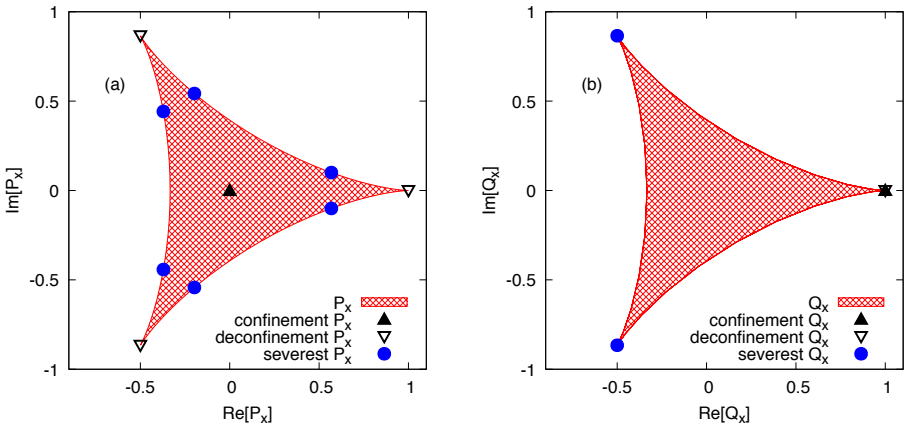

Figure 2.2: Allowed region of (a) $P_{\boldsymbol{x}}$ and (b) $Q_{\boldsymbol{x}}$. The filled triangle and three vertices are the confined and deconfined states, respectively. These points degenerate at $Q_{\boldsymbol{x}} = 1$ in (b). The filled circles correspond to configurations $(\varphi_{r,\boldsymbol{x}}, \varphi_{g,\boldsymbol{x}}, \varphi_{b,\boldsymbol{x}}) = (\pm 2\pi/9, \pm 2\pi/9, \mp 4\pi/9)$ and their $\mathbb{Z}_3$ and/or Weyl-symmetry transformed ones.

2.2.3 Fermion potential in EPL model

Here, we study properties of the fermionic Lagrangian density in EPLMWO and $\mathbb{Z}_3$-EPLM. For each fermionic Lagrangian density, the reality in the finite chemical potential region is not ensured, since $P_{\boldsymbol{x}}$ and $Q_{\boldsymbol{x}}$ are generally complex. Here, for simplicity, we discuss the sign problem in EPLMWO and $\mathbb{Z}_3$-EPLM with the real part of the fermionic Lagrangian density only. In the calculations, we set $M/T = 10$ and $\mu/M = 0.5, 1.0$ and 1.5.

Figure 2.3 shows $\mathrm{Re}[L_F]$ of EPLMWO in the $\varphi_{r,\boldsymbol{x}}$–$\varphi_{g,\boldsymbol{x}}$ plane. It is seen that $\mathrm{Re}[L_F]$ is minimum at the configuration $(\varphi_{r,\boldsymbol{x}}, \varphi_{g,\boldsymbol{x}}) = (0, 0)$ corresponding to $P_{\boldsymbol{x}} = 1$, and the result at $\mu/M = 1.5$ is qualitatively the same as at $\mu/M = 0.5$ due to the particle-hole symmetry. Thus, stochastically, the state $P_{\boldsymbol{x}} = 1$ is more favorable than other states. Furthermore, the $\mathbb{Z}_3$ images of the origin, $(\varphi_{r,\boldsymbol{x}}, \varphi_{g,\boldsymbol{x}}) = (\pm 2\pi/3, \pm 2\pi/3)$ corresponding to $P_{\boldsymbol{x}} = e^{\pm i2\pi/3}$, have a lower probability than $P_{\boldsymbol{x}} = 1$, since $\mathbb{Z}_3$ symmetry is explicitly broken in EPLMWO.

Figure 2.4 shows $\mathrm{Re}[L_{F,\mathbb{Z}_3}]$ of $\mathbb{Z}_3$-EPLM in the $\varphi_{r,\boldsymbol{x}}$–$\varphi_{g,\boldsymbol{x}}$ plane. There are nine minimum points in both panels (a) and (c), and the result (c) is qualitatively same as the result (a). Of the nine minimum points, the configurations $(\varphi_{r,\boldsymbol{x}}, \varphi_{g,\boldsymbol{x}}) = \{(\pm 2\pi/3, \pm 2\pi/3), (0, 0)\}$ correspond to the deconfined states, and other six points, $(\varphi_{r,\boldsymbol{x}}, \varphi_{g,\boldsymbol{x}}) = \{(\pm 2\pi/3, \mp 2\pi/3), (\pm 2\pi/3, 0), (0, \pm 2\pi/3)\}$, mean the confinement configurations. From these situations, both confined and deconfined states are degenerate in this model.

Figure 2.5 shows the effective potential from the Haar measure L_H in the $\varphi_{r,\boldsymbol{x}}$–$\varphi_{g,\boldsymbol{x}}$ plane. It is clearly seen that L_H has minima at the confined states, and this result indicates that the confined states are stochastically favored

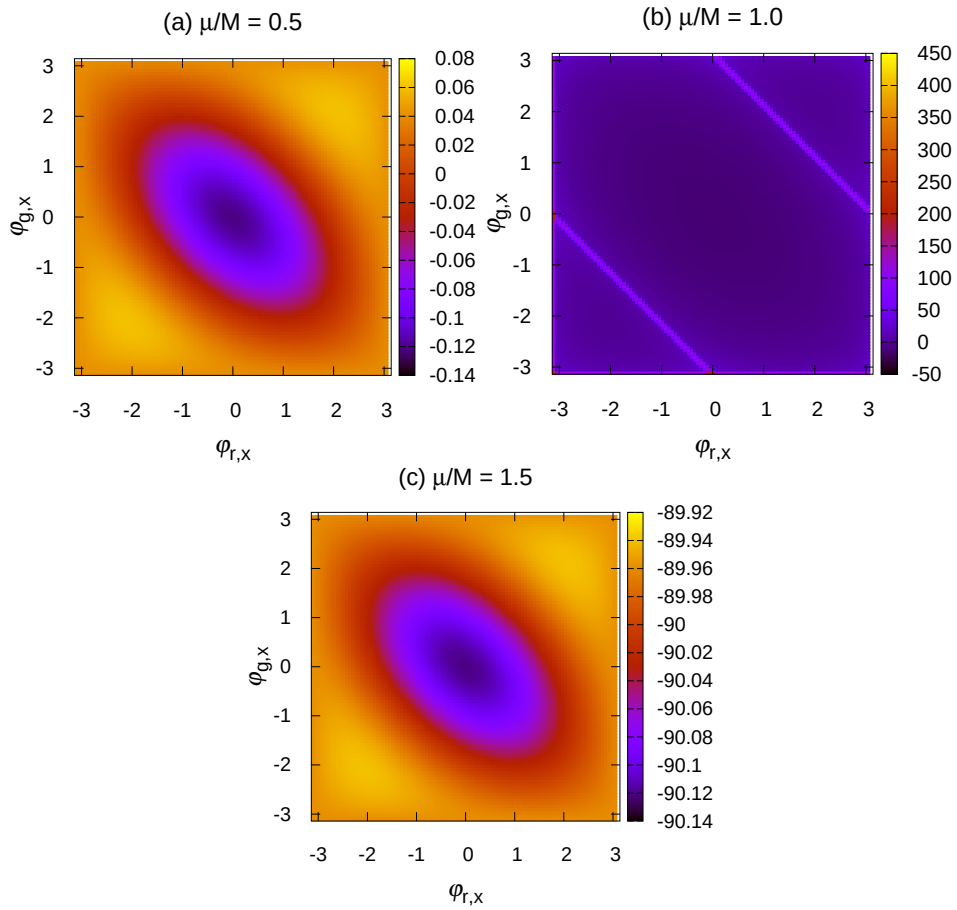

Figure 2.3: $\mathrm{Re}[L_F]$ in the $\varphi_{r,\boldsymbol{x}}$–$\varphi_{g,\boldsymbol{x}}$ plane. In the calculations, we set $M/T = 10$ and (a) $\mu/M = 0.5$, (b) $\mu/M = 1.0$, and (c) $\mu/M = 1.5$ respectively.

due to the effective potential L_H.

Let us consider two models with $N_s = 1$, where the kinetic term is absent and the fermionic Lagrangian density L_F (or $L_{F,\mathbb{Z}_3}$) and L_H are dominant. In $\mathbb{Z}_3$-EPLM, as mentioned above, $L_{F,\mathbb{Z}_3}$ favors both confined and deconfined states, while L_H does the confined state. Hence, the confined state is favored in $\mathbb{Z}_3$-EPLM with $N_s = 1$.

On the other hand, in EPLMWO with $N_s = 1$, L_F favors the deconfined state, so that the situation is more complicated. The favored state depends on parameters. To see the dependence of parameters M and μ, we consider the following quantity

$$\begin{aligned}\Delta L_{F,R} &= \mathrm{Re}\left[L_F|_{P_{\boldsymbol{x}}=0} - L_F|_{P_{\boldsymbol{x}}=1}\right] \\ &= -2N_f \left[\log \frac{1+e^{3(\mu-M)/T}}{1+e^{(\mu-M)/T}+e^{2(\mu-M)/T}+e^{3(\mu-M)/T}}\right. \\ &\qquad \left. + \log \frac{1+e^{-3(\mu+M)/T}}{1+e^{-(\mu+M)/T}+e^{-2(\mu+M)/T}+e^{-3(\mu+M)/T}}\right]. \end{aligned} \tag{2.20}$$

The μ/M-dependence of $\Delta L_{F,R}$ is shown in Fig. 2.6. It is seen that $\Delta L_{F,R}$ becomes large around $\mu/M \sim 1$, while it is suppressed in $\mu/M < 0.5$ and

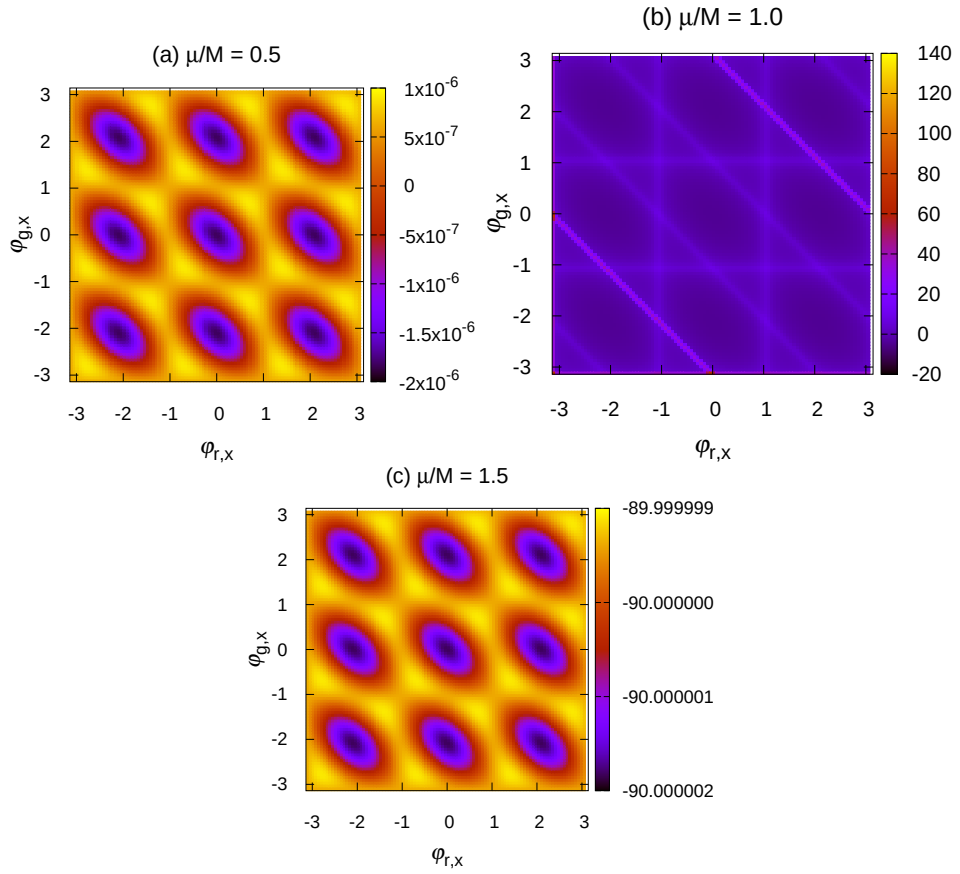

Figure 2.4: $\mathrm{Re}[L_{F,\mathbb{Z}_3}]$ in the $\varphi_{r,\boldsymbol{x}}$–$\varphi_{g,\boldsymbol{x}}$ plane. In the calculations, we set $M/T = 10$ and (a) $\mu/M = 0.5$, (b) $\mu/M = 1.0$, and (c) $\mu/M = 1.5$ respectively.

$\mu/M > 1.5$. This indicates that the deconfined state $P_{\boldsymbol{x}} = 1$ is favored when $\Delta L_{F,R}$ is large. Therefore, the deconfined state is favorably realized at $\mu/M \sim 1$.

In the EPL model with $N_s > 1$, the gluon kinetic term S_G exists, and this term favors the deconfined state when κ is large. Thus, at large κ, the absolute value of the spatial average of Polyakov line

$$\bar{P} \equiv \frac{1}{V} \sum_{\boldsymbol{x}} P_{\boldsymbol{x}} \tag{2.21}$$

has a finite value. On the other hand, at small κ, the effect of favoring the deconfined state is weak, and $P_{\boldsymbol{x}}$ is spread in the complex plane. Hence, the cancellation occurs and the spatial average $\bar{P}$ becomes zero.

The relations of $\mathrm{Re}[L_F]$–$\mathrm{Im}[L_F]$ and $\mathrm{Re}[L_{F,\mathbb{Z}_3}]$–$\mathrm{Im}[L_{F,\mathbb{Z}_3}]$ in the case of $N_f = 3$ are shown in Fig. 2.7. Here, we set $M/T = 10$ and $\mu/M = 0.95$, where the sign problem is considered to be serious. As for EPLMWO, in the left panel of Fig. 2.7, the maximum of $|\mathrm{Im}[L_F]|$ is much larger than $\pi/2$. This result indicates that we cannot determine the sign of $\cos(\mathrm{Im}[S])$, and the sign problem becomes more serious. On the other hand, the maximum of

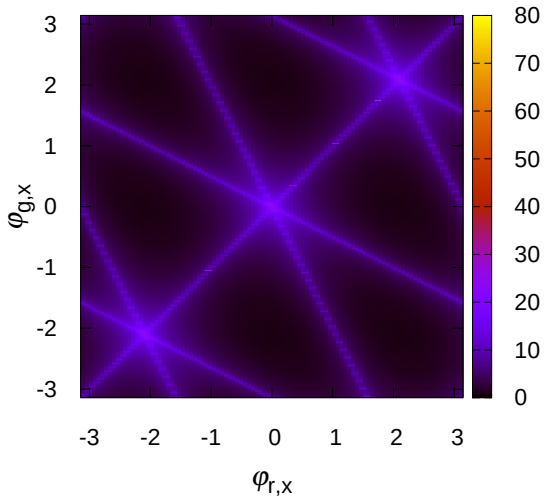

Figure 2.5: Effective potential L_H from the Haar measure in $\varphi_{r,\boldsymbol{x}}$–$\varphi_{g,\boldsymbol{x}}$ plane.

$|\mathrm{Im}[L_{F,\mathbb{Z}_3}]|$ is smaller than $\pi/2$ in $\mathbb{Z}_3$-EPLM. Thus, there is no sign problem at $\mu/M = 0.95$ with $N_s = 1$, since $\cos(\mathrm{Im}[L_{F,\mathbb{Z}_3}])$ is always positive. However, in $\mathbb{Z}_3$-EPLM with $N_s > 1$, the absolute value of $S_{F,\mathbb{Z}_3} = \sum_{\boldsymbol{x}} L_{F,\mathbb{Z}_3}$ can have the larger value than $\pi/2$, so that $\cos(\mathrm{Im}[S_{F,\mathbb{Z}_3}])$ can have negative sign. In this situation, the sign problem exists, but it is expected to be milder in $\mathbb{Z}_3$-EPLM than in EPLMWO.

2.3 Reweighting method

In this study, the configuration φ is generated by using the importance sampling with the probability weight $F[\varphi]$, and the expectation value of the operator $\hat{\mathcal{O}}$ is derived by

$$\langle \mathcal{O} \rangle = \frac{1}{Z} \int \mathcal{D}\varphi \ \hat{\mathcal{O}} F[\varphi], \quad Z = \int \mathcal{D}\varphi \ F[\varphi], \ F[\varphi] = e^{-S}. \tag{2.22}$$

When $F[\varphi]$ is complex, the sign problem occurs and we cannot carry out the importance sampling. To avoid this problem, the approximated probability weight $F'[\varphi] \in \mathbb{R}$ is introduced, and the expectation value is rewritten as

$$\langle \mathcal{O} \rangle = \frac{\langle \mathcal{O} \cdot F/F' \rangle'}{W}, \ W = \langle F/F' \rangle', \tag{2.23}$$

$$\langle \mathcal{O} \rangle' = \frac{1}{Z'} \int \mathcal{D}\varphi \ \hat{\mathcal{O}} F'[\varphi], \quad Z' = \int \mathcal{D}\varphi \ F'[\varphi], \tag{2.24}$$

where W is called the reweighting factor. By using this relation, we can measure the expectation value $\langle \mathcal{O} \rangle$ through the configurations generated with $F'[\varphi]$. This is called reweighting method [58], and widely used to calculate observables of LQCD simulations in the finite μ region.

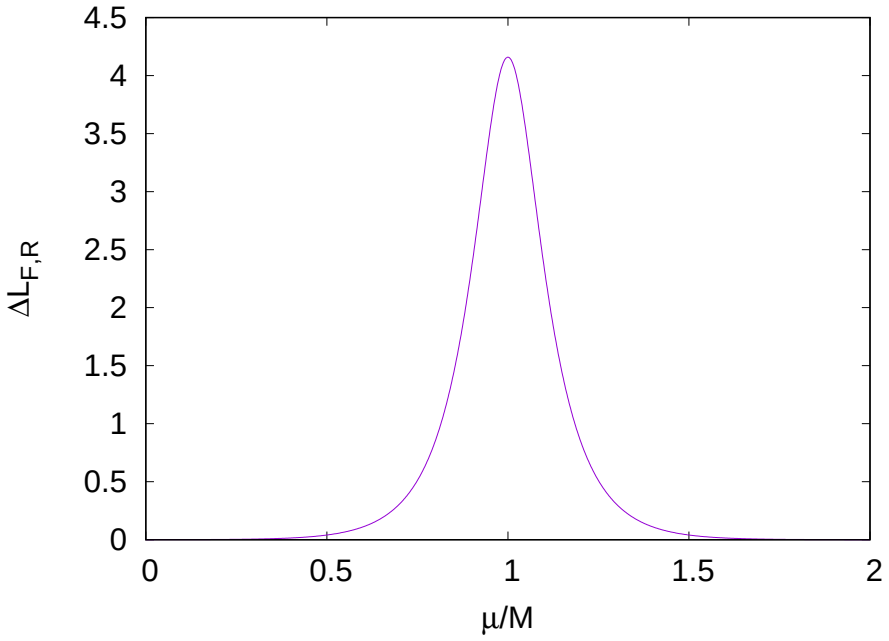

Figure 2.6: μ/M-dependence of $\Delta L_{F,R}$.

Eq. (2.23) is mathematically correct. However, the expectation value $\langle \mathcal{O} \rangle$ is unreliable, when the factor W has a tiny value and the statistical error of $\langle \mathcal{O} \rangle$ becomes large. This situation occurs when the sign problem exists and is serious. Therefore, we can use the factor W as an indicator for the seriousness of the sign problem.

2.3.1 Phase quenched approximation

The most simplest selection of $F'[\varphi]$ is the following:

$$F'[\varphi] = |F[\varphi]| = e^{-\mathrm{Re}[S]}. \tag{2.25}$$

This is called the phase quenched approximation. Here, we ignore the imaginary part of the action and generate configuration with the probability weight $e^{-\mathrm{Re}[S]}$. By using this, we measure the expectation value $\langle \mathcal{O} \rangle$ and the reweighting factor W' with

$$\langle \mathcal{O} \rangle = \frac{\langle \mathcal{O} \cdot e^{-i\mathrm{Im}[S]} \rangle'}{W'}, \ W' = \langle e^{-i\mathrm{Im}[S]} \rangle', \tag{2.26}$$

$$\langle \mathcal{O} \rangle' = \frac{1}{Z'} \int \mathcal{D}\varphi \ \mathcal{O} F'[\varphi], \ Z' = \int \mathcal{D}\varphi \ F'[\varphi]. \tag{2.27}$$

In this study, we refer to the reweighting method with the phase quenched approximation as the phase quenched reweighting (PQRW).

According to Ref. [17], after taking the partial average of the configuration φ and the charge conjugated one, the factor W' becomes

$$W' = \int \mathcal{D}\varphi \ \cos\left(\mathrm{Im}[S]\right) F'[\varphi] = \langle \cos\left(\mathrm{Im}[S]\right) \rangle', \tag{2.28}$$

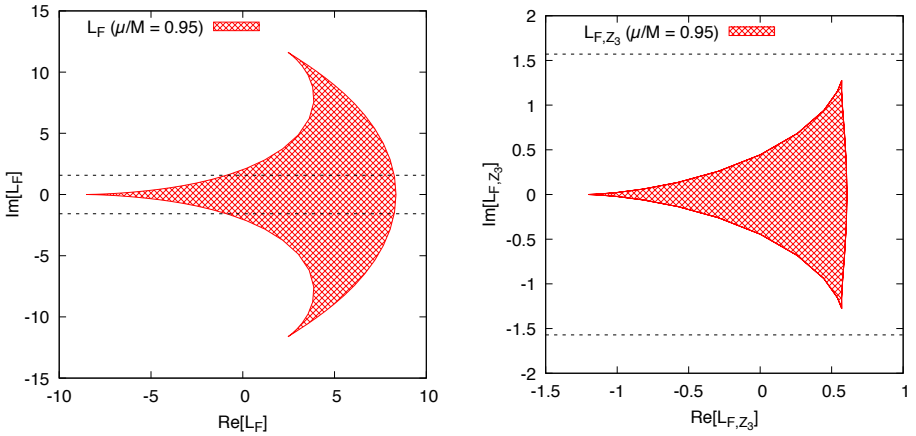

Figure 2.7: (left) $\mathrm{Re}[L_F]$–$\mathrm{Im}[L_F]$ or (right) $\mathrm{Re}[L_{F,\mathbb{Z}_3}]$–$\mathrm{Im}[L_{F,\mathbb{Z}_3}]$ relation in the case of $N_f = 3$. We set $M/T = 10$ and $\mu/M = 0.95$. The two dashed lines are drawn at $\pm\pi/2$, respectively.

since $\mathrm{Im}\left[S[\varphi]\right] = -\mathrm{Im}\left[S[\varphi']\right]$. Therefore, $W' \in \mathbb{R}$ and $|W'| \leq 1$ are ensured. If $\cos\left(\mathrm{Im}[S]\right)$ has a negative value, a cancellation between the configuration with the positive $\cos\left(\mathrm{Im}[S]\right)$ and that with the negative one occurs, and then the absolute value of W' becomes small. In this situation, the smallness of $|W'|$ makes the statistical error large due to the error propagation.

2.3.2 Improved phase quenched approximation

In Ref. [59], the distribution of the complex phase of the quark determinant is studied by using the Taylor expansion method, and it is well approximated by a Gaussian distribution function. Hence, in order to improve PQRW, we consider the following new approximated probability weight:

$$F''[\varphi] = \exp\left[-\mathrm{Re}[S] - \alpha\left(\mathrm{Im}[S]\right)^2\right], \tag{2.29}$$

where α is the parameter that may depend on κ, μ and N_s in the EPL model. By using the new approximated probability weight, we can measure the expectation value $\langle\mathcal{O}\rangle$ and the reweighting factor W'' with

$$\langle\mathcal{O}\rangle = \frac{\left\langle\mathcal{O}\cdot\exp\left[-i\mathrm{Im}[S] + \alpha\left(\mathrm{Im}[S]\right)^2\right]\right\rangle''}{W''}, \tag{2.30}$$

$$W'' = \left\langle\exp\left[-i\mathrm{Im}[S] + \alpha\left(\mathrm{Im}[S]\right)^2\right]\right\rangle'', \tag{2.31}$$

$$\langle\mathcal{O}\rangle'' = \frac{1}{Z''}\int\mathcal{D}\varphi\ \mathcal{O}F''[\varphi],\ Z'' = \int\mathcal{D}\varphi\ F''[\varphi]. \tag{2.32}$$

In this study, we refer to this reweighting method as the improved phase quenched reweighting (IPQRW).

After taking the partial average as in Eq. (2.28), the factor W'' becomes

$$W'' = \frac{1}{Z''}\int \mathcal{D}\varphi \ \cos\left(\mathrm{Im}[S]\right) e^{\alpha(\mathrm{Im}[S])^2} = \left\langle \cos\left(\mathrm{Im}[S]\right) \exp\left[\alpha\left(\mathrm{Im}[S]\right)^2\right]\right\rangle''. \tag{2.33}$$

Hence, W'' is real but $|W''| \leq 1$ is not ensured in this case. If $\mathrm{Im}[S] \ll 1$, it is expected that $W'' \sim \tilde{W}'' \equiv \langle e^{\alpha(\mathrm{Im}[S])^2}\rangle'' \geq 1$. To see the seriousness of the sign problem with IPQRW, we use $W''/\tilde{W}''$ instead of W''.

2.4 Numerical results

In this section, we show numerical results by using PQRW and IPQRW in both EPLMWO and $\mathbb{Z}_3$-EPLM. We utilize the standard Monte Carlo simulation to generate configurations, and consider 3 cases of the spatial lattice extents, $N_s = 6, 8$, and 12 with $M/T = 10$. For each parameter set, we use 500 configurations to measure the observables.

Here, we measure expectation values of the reweighting factors W' and W'', the spatial averaged Polyakov line shown in Eq. (2.21), and the quark number density given by

$$n_q = \frac{T}{V}\frac{\partial}{\partial\mu}\log Z = \frac{1}{N_s^3}\frac{\partial}{\partial(\mu/T)}\log Z. \tag{2.34}$$

In LQCD simulation at finite μ with PQRW, the quark number density becomes zero for $\mu < m_\pi/2$ (the Silver Blaze problem [60]), and the early onset occurs at $\mu = m_\pi/2$ [61–64], where m_π denotes the pion mass. Hence, we can use n_q to check the reliability of the numerical simulation of the EPL model.

2.4.1 Results of $\mathbb{Z}_3$-EPLM at $\mu = 0$

At first, we consider the case of $\mu/M = 0$ and set $N_s = 6$. Here, the sign problem does not occur in the EPL model, so that the reweighting method is not needed. Figure 2.8 shows the κ-dependence of the expectation value of $|\bar{P}|$. In the low temperature region ($\kappa < 0.13$), $\langle|\bar{P}|\rangle$ has a tiny value, while $\langle|\hat{P}|\rangle > 0.5$ in the high temperature region ($\kappa > 0.13$). The rapid change of $\langle|\bar{P}|\rangle$ occurs at $\kappa \sim 0.13$, and this indicates the first-order phase transition. However, we don't discuss the order of the transition, since N_s we use is not large enough to determine the order.

In Fig. 2.9, the sample scatter plots of $P_{\boldsymbol{x}}$ for $\mathbb{Z}_3$-EPLM at $\kappa = 0$ and 0.5 in one configuration are shown. At $\kappa = 0$ (the low temperature region), $P_{\boldsymbol{x}}$ is widely spread in the complex plane, and the spatial average of $P_{\boldsymbol{x}}$ becomes almost zero. On the other hand, at $\kappa = 0.5$ (the high temperature region), $P_{\boldsymbol{x}}$ are distributed around $P_{\boldsymbol{x}} \sim 1, e^{\pm i2\pi/3}$ and the spatial average becomes $\bar{P} \sim 1, e^{\pm i2\pi/3}$.

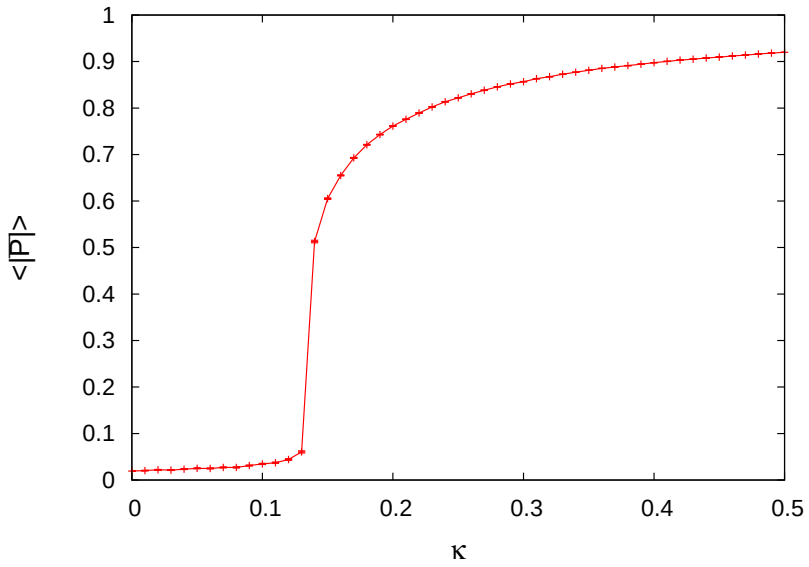

Figure 2.8: κ-dependence of the expectation value of $|\bar{P}|$ at $\mu = 0$.

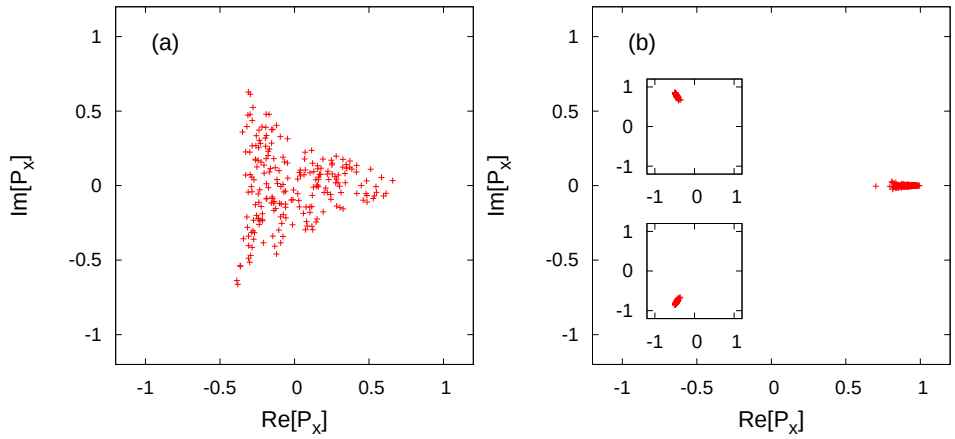

Figure 2.9: Scatter plot of $P_{\boldsymbol{x}}$ at (a) $\kappa = 0$ and (b) $\kappa = 0.5$ in one configuration. We set $N_s = 6$. Two small windows in the right panel show the scatter plot in other configurations.

In EPLMWO with $M/T = 10$, the similar results are obtained, since the effect of the fermion action is small and $\mathbb{Z}_3$ symmetry is almost preserved. If we set $M/T = 5$, where the quark mass is smaller than that in $M/T = 10$, $\mathbb{Z}_3$ symmetry is broken and the quark contribution L_F favors the state $P_{\boldsymbol{x}} = 1$. Therefore, $P_{\boldsymbol{x}}$ at the large κ are distributed around only $P_{\boldsymbol{x}} \sim 1$.

2.4.2 Results of PQRW

EPLMWO and $\mathbb{Z}_3$-EPLM have the sign problem in the finite quark chemical potential region. Here, we use PQRW to calculate the reweighting factor and compare the results in $\mathbb{Z}_3$-EPLM with that in EPLMWO. To compute the reweighting factor W', we set $N_s = 6$ here.

Figure 2.10 shows the κ- and μ-dependence of the reweighting factor W'.

The left panel of Fig. 2.10 shows the result in EPLMWO, and the right panel corresponds to $\mathbb{Z}_3$-EPLM. In both the panels, due to the particle-hole symmetry, the behavior of the reweighting factor is almost symmetric with respect to the line of $\mu = M$.

In the left panel of Fig. 2.10, for EPLMWO, the sign problem is serious in the region $0.5 \lesssim \mu/M \lesssim 1.5$ and $\kappa < 0.15$. At $\mu = M$, the fermion Lagrangian density L_F is almost real, and the reweighting factor W' becomes almost 1.

In the right panel of Fig. 2.10, for $\mathbb{Z}_3$-EPLM, the reweighting factor W' is almost zero only in the region $0.85 \lesssim \mu/M \lesssim 1.15$. In the regions $0.5 \lesssim \mu/M \lesssim 0.85$, $1.15 \lesssim \mu/M \lesssim 1.5$ and $\kappa < 0.15$, the sign problem in $\mathbb{Z}_3$-EPLM is considered to be less serious than in EPLMWO, since the reweighting factor is much larger than in EPLMWO. At $\mu = M$, the reweighting factor is almost 1 and the sign problem does not occur, since the fermion Lagrangian $L_{F,\mathbb{Z}_3}$ is almost real as in the case of EPLMWO.

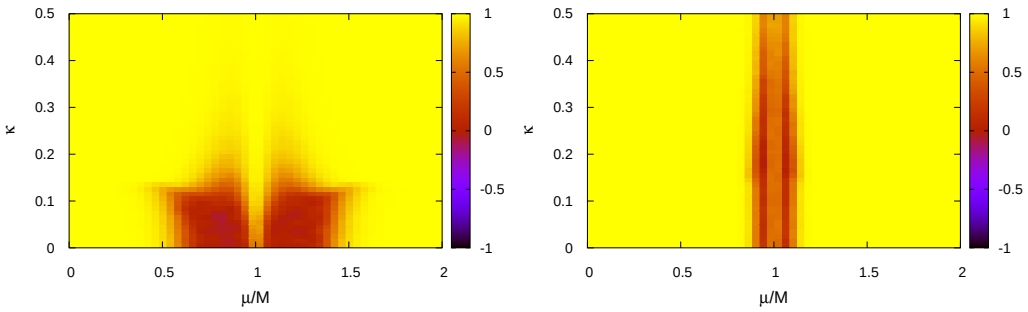

Figure 2.10: κ- and μ-dependence of the reweighting factor for EPLMWO (left) and $\mathbb{Z}_3$-EPLM (right).

2.4.3 Results of IPQRW

Here, we carry out the new reweighting method we improved, and compare them with the results measured by PQRW.

At first, we set $N_s = 6$ and calculate the ratio $W''/\tilde{W}''$. In Fig. 2.11, the κ- and μ-dependence of $W''/\tilde{W}''$ are shown. The left panel shows the result in EPLMWO, and the right panel does that in $\mathbb{Z}_3$-EPLM. In both the panels, it is seen that $W''/\tilde{W}''$ is smaller than 1 but is larger than the factor W' obtained by using PQRW. These results indicate that IPQRW makes the sign problem much milder than PQRW.

Now, we compare the results of PQRW and IPQRW in both EPLMWO and $\mathbb{Z}_3$-EPLM. Figure 2.12 shows the μ- and N_s-dependence of the reweighting factor in EPLMWO and $\mathbb{Z}_3$-EPLM. We can confirm that the reweighting factors of both PQRW and IPQRW are almost 1 at $\mu = M$, thus it is considered that the sign problem in both the EPL models vanishes almost

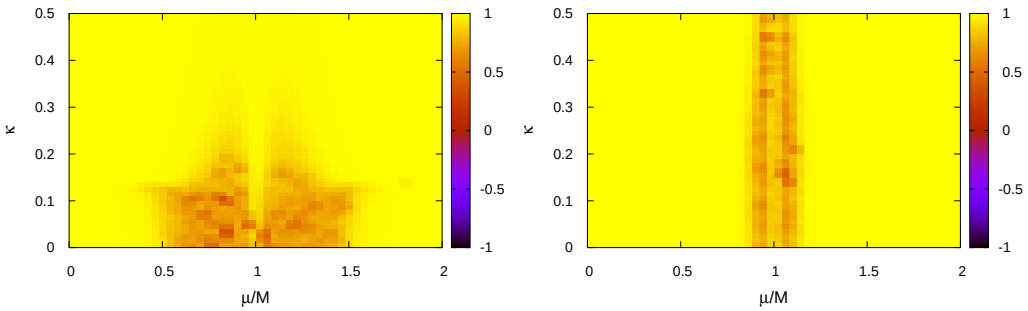

Figure 2.11: κ- and μ-dependence of the ratio $W''/\tilde{W}''$ for EPLMWO (left) and $\mathbb{Z}_3$-EPLM (right). We set $\alpha = 3.5$.

completely there. It is also seen that the factors of IPQRW in both the models have larger values than that of PQRW in the region where the sign problem is serious in PQRW. For the N_s-dependence, the region where the reweighting factors depart from 1 becomes wider as N_s increases.

In Fig. 2.13, the results of the expectation value of $|\bar{P}|$ are shown. When using PQRW, the statistical error becomes large in the region where the sign problem is serious. On the other hand, when using IPQRW in both the EPL models, the expectation value has the much smaller error than that obtained by PQRW in the same region. This result indicates that IPQRW makes the sign problem much milder than PQRW. It is also seen that the expectation value $\langle|\bar{P}|\rangle$ is almost independent of the lattice extent N_s.

Figure 2.14 shows the results of the quark number density n_q. In both the EPL models, it is seen that the value of n_q is almost zero in $\mu/M \lesssim 0.6$ for EPLMWO and $\mu \lesssim 0.9$ for $\mathbb{Z}_3$-EPLM, while $n_q \sim 18$ in $\mu/M \gtrsim 1.4$ for EPLMWO and $\mu/M \gtrsim 1.1$ for $\mathbb{Z}_3$-EPLM. The value $n_q \sim 18$ is the degree of freedom of quarks. Where the sign problem is serious, the statistical error is large in both the EPL models. Comparing the results with different N_s, we cannot see the N_s-dependence in both the EPL models. Around $\mu/M \sim 1$, the value in $\mathbb{Z}_3$-EPLM changes more rapidly than that in EPLMWO. It is considered that this occurs since $\mathbb{Z}_3$-EPLM has the explicit $\mathbb{Z}_3$ symmetry.

2.4.4 EPLMWO and $\mathbb{Z}_3$-EPLM with large M/T

So far, we fix the ratio $M/T = 10$ for κ corresponding to temperature T. However, when T is small, M/T will become large. To check the consistency between EPLMWO and $\mathbb{Z}_3$-EPLM in the limit $T \to 0$, we set $M/T = 30$ and $\kappa = 0.0$, and calculate the reweighting factor W' and the quark number density n_q with PQRW. These results in both the EPL models are shown in Fig. 2.15. The left panel shows the result of W'. It is seen that the reweighting factors in both the models are smaller than 1 in almost the same region, but the factor has larger value in $\mathbb{Z}_3$-EPLM than in EPLMWO. Thus,

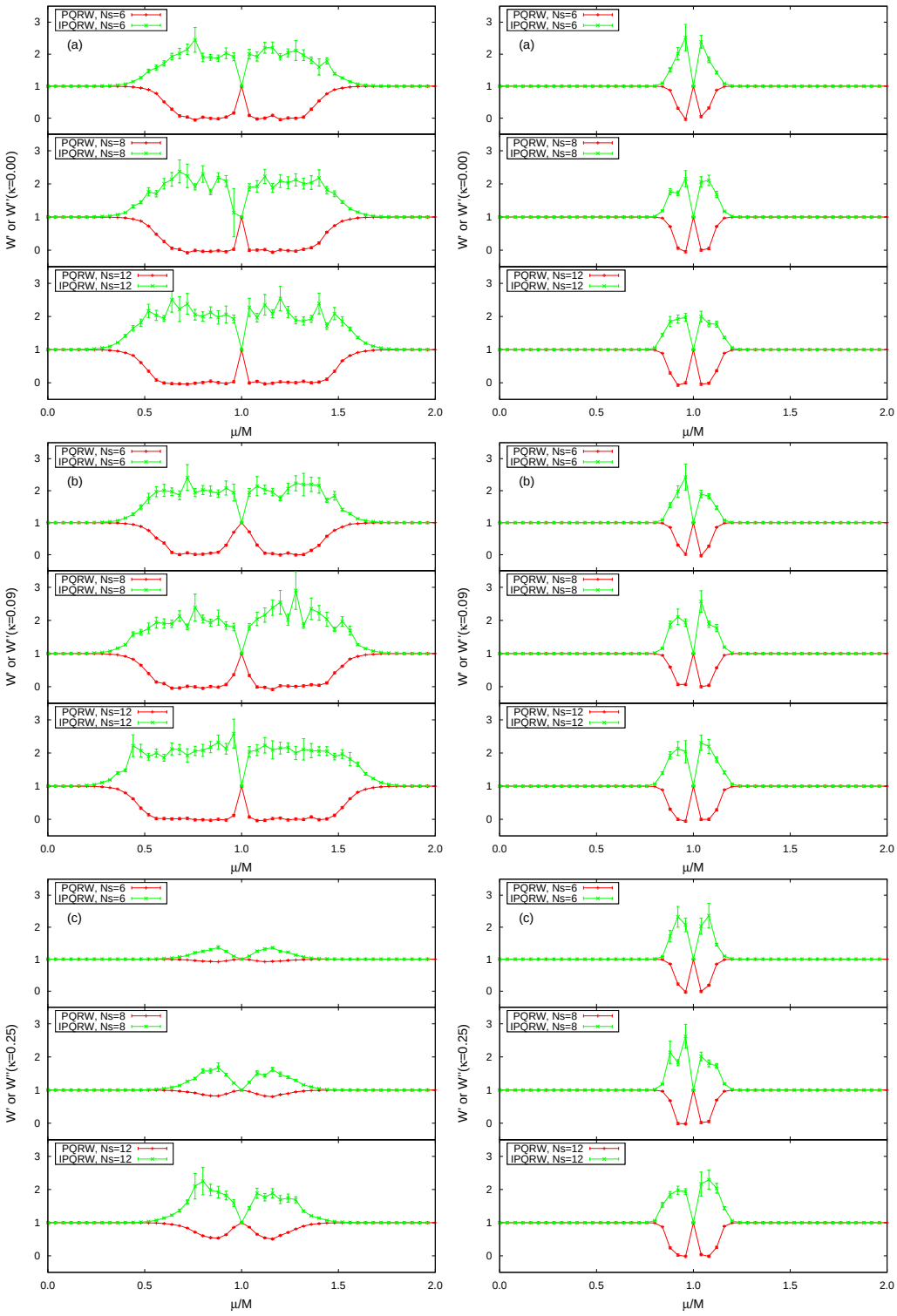

Figure 2.12: μ- and N_s-dependence of the reweighting factors (W' and W'') in (left) EPLMWO and (right) $\mathbb{Z}_3$-EPLM with both PQRW and IPQRW. In all panels, red (green) symbols denote the results obtained with PQRW (IPQRW). (a) $\kappa = 0.0$, (b) $\kappa = 0.09$, and (c) $\kappa = 0.25$.

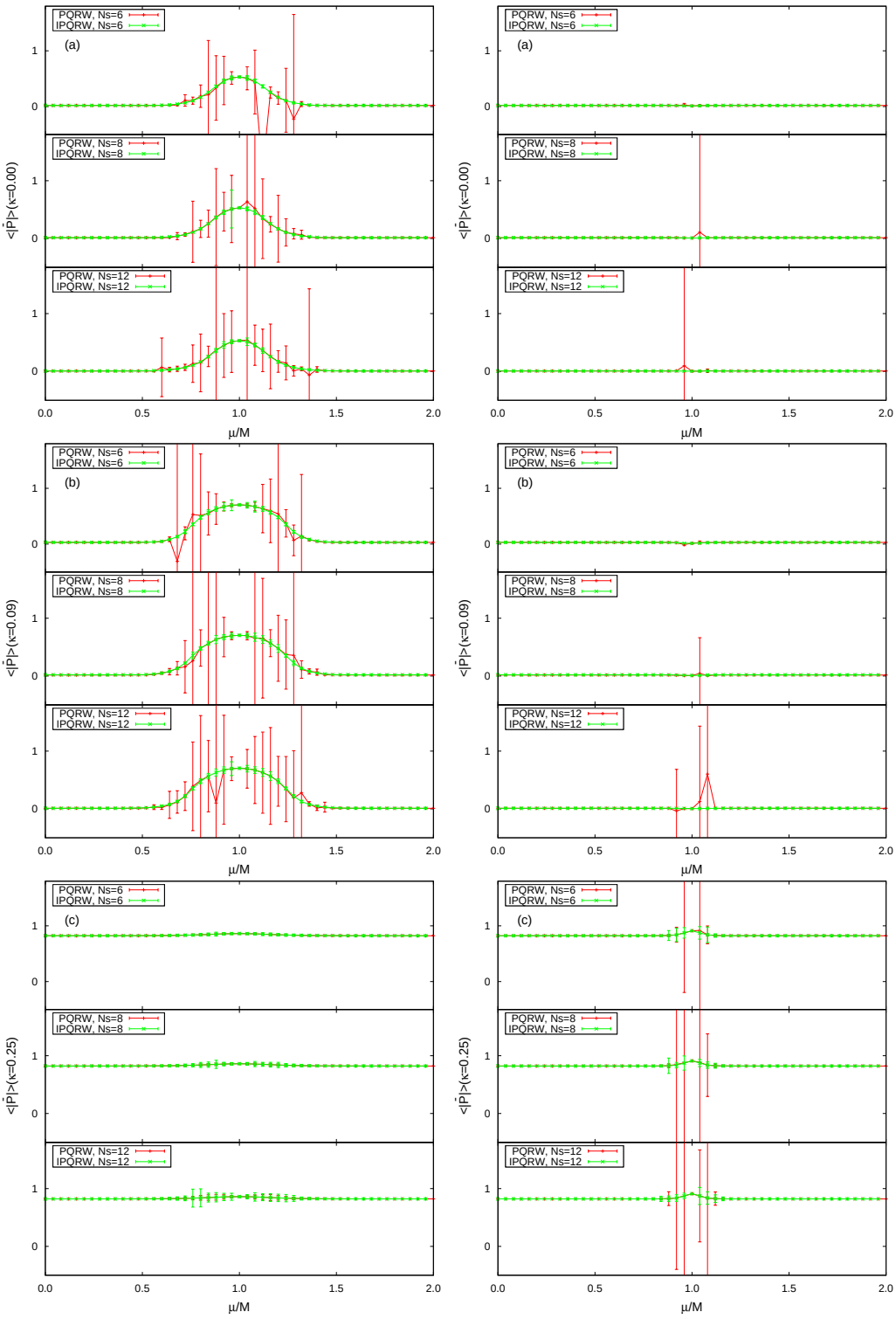

Figure 2.13: μ- and N_s-dependence of $\langle|\bar{P}|\rangle$ in (left) EPLMWO and (right) $\mathbb{Z}_3$-EPLM with both PQRW and IPQRW. In all panels, red (green) symbols denote the results obtained with PQRW (IPQRW). (a) $\kappa = 0.0$, (b) $\kappa = 0.09$, and (c) $\kappa = 0.25$.

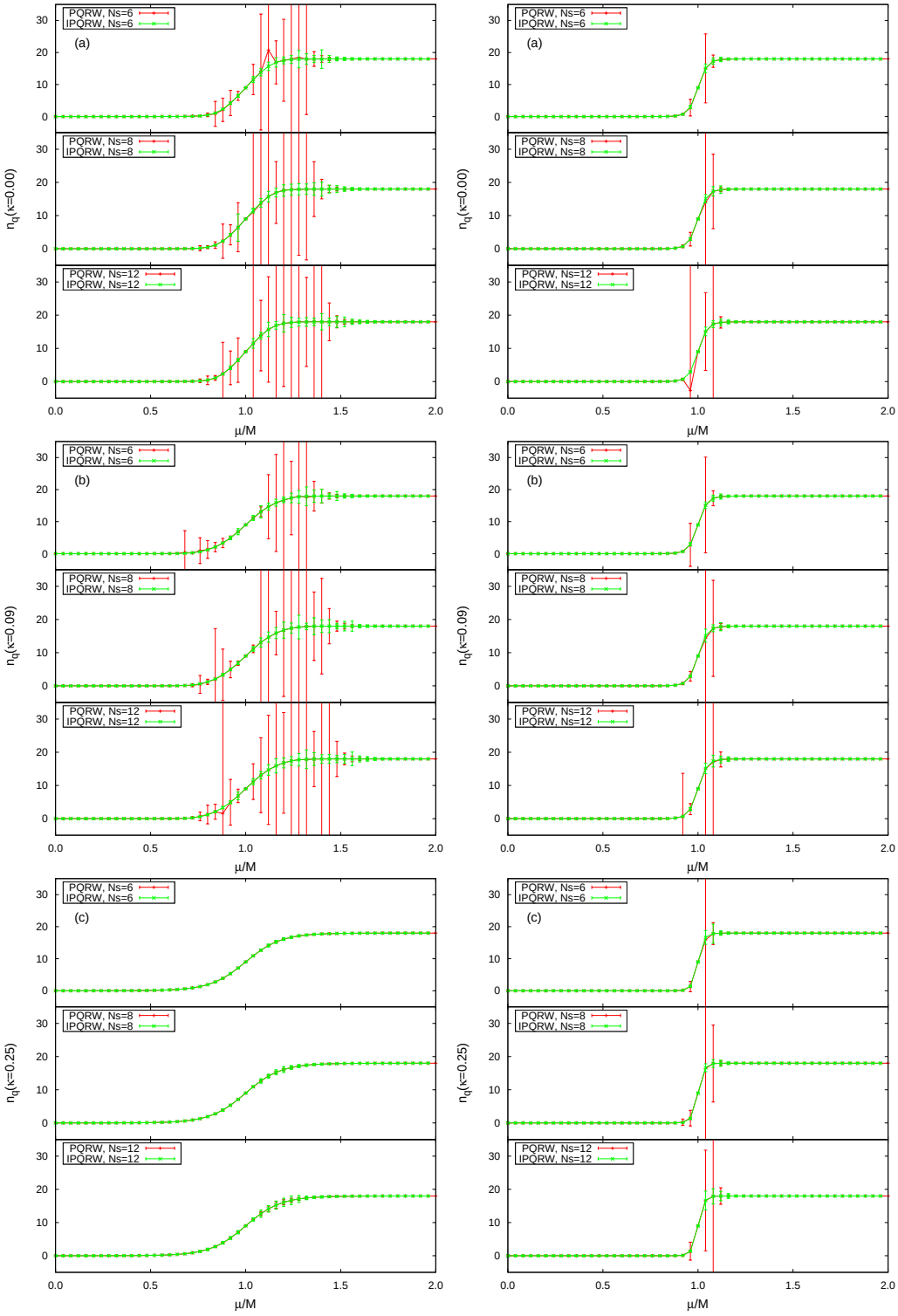

Figure 2.14: μ- and N_s-dependence of n_q in (left) EPLMWO and (right) $\mathbb{Z}_3$-EPLM with both PQRW and IPQRW. In all panels, red (green) symbols denote the results obtained with PQRW (IPQRW). (a) $\kappa = 0.0$, (b) $\kappa = 0.09$, and (c) $\kappa = 0.25$.

the sign problem of $\mathbb{Z}_3$-EPLM with $M/T = 30$ is much milder in all μ/M.

In the right panel of Fig. 2.15, the results of n_q in both the EPL models are shown. It is easily seen that the result in EPLMWO has the large statistical error meaning the fact that the sign problem is serious, while that in $\mathbb{Z}_3$-EPLM has the small error in all μ/M. Comparing the results in both the models, n_q in $\mathbb{Z}_3$-EPLM is consistent with that in EPLMWO when the sign problem of EPLMWO is not serious. This indicates that $\mathbb{Z}_3$-EPLM in the limit $T \to 0$ agrees with EPLMWO. It is also seen that the behavior of n_q in $\mathbb{Z}_3$-EPLM is similar to the step function $18\Theta(\mu - M)$. Therefore, it is considered that there is no early onset of n_q in the low temperature region for $\mathbb{Z}_3$-EPLM.

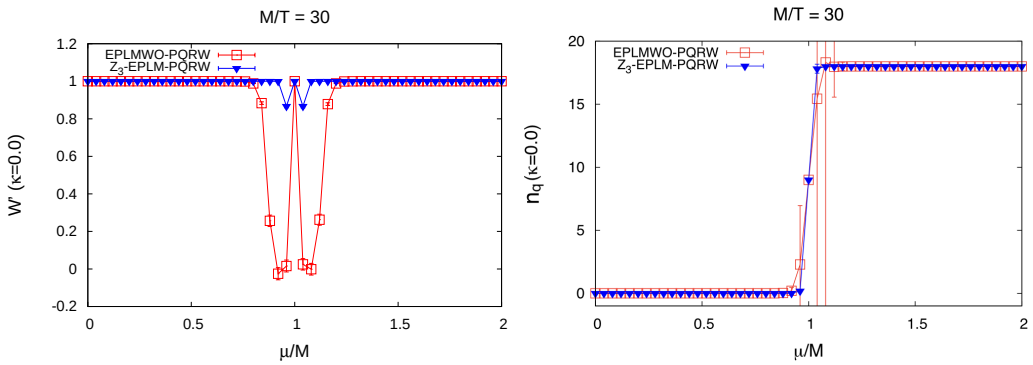

Figure 2.15: μ-dependence of (left) W' and (right) n_q in EPLMWO and $\mathbb{Z}_3$-EPLM with $M/T = 30$ at $\kappa = 0.0$. Here, we use PQRW.

2.5 Short summary

In order to investigate the relation between exact $\mathbb{Z}_3$ symmetry and the sign problem in QCD, we use EPLMWO as an effective model of LQCD, and construct the $\mathbb{Z}_3$-EPLM corresponding to $\mathbb{Z}_3$-QCD. We make numerical simulations of both the EPL models by using the reweighting method with the phase quenched approximation, and compare the results.

Our results show that the region where the sign problem is serious becomes much narrower by introducing exact $\mathbb{Z}_3$ symmetry to the model. Due to this, the statistical error of expectation values becomes smaller in $\mathbb{Z}_3$-EPLM. These results indicate that the sign problem is milder in $\mathbb{Z}_3$-EPLM than in EPLMWO. Therefore, it is expected that lattice calculations of $\mathbb{Z}_3$-QCD are possible in the wider quark chemical potential region than of the ordinary QCD.

In this study, we also propose the improved reweighting method with the contribution of the imaginary part of the effective action. With this new method in both the EPL models, the reweighting factor becomes larger than 1, when the sign problem is serious in PQRW. Thus, the new method

we proposed makes the sign problem much weaker. Moreover, in LQCD calculations with PQRW for the finite isospin quark chemical potential, the pion condensation occurs and it makes the sign problem too difficult. Hence, our improved method including the imaginary part of the lattice action may make it possible to avoid this problem in the lattice calculations.

In the small temperature limit, the result of the quark number density n_q in $\mathbb{Z}_3$-EPLM almost agrees with in EPLMWO, and there is no early onset of n_q in $\mathbb{Z}_3$-EPLM. However, the early-onset problem in $\mathbb{Z}_3$-EPLM may be different from $\mathbb{Z}_3$-QCD, since the EPL model is constructed in the heavy quark mass limit and the chiral dynamics is not taken into account. Therefore, it is also needed to check whether or not the early onset of n_q occurs in the lattice calculation of $\mathbb{Z}_3$-QCD.

Chapter 3

Analyses of pure SU(2) gauge theory

3.1 Gradient flow method

The gradient flow equation for pure SU(N_c) gauge theory [42] is defined by

$$\partial_t B_\mu(t,x) = D_\nu G_{\nu\mu}(t,x), \quad B_\mu(t=0,x) = A_\mu(x), \tag{3.1}$$

$$D_\mu = \partial_\mu + [B_\mu, \cdot], \tag{3.2}$$

$$G_{\mu\nu}(t,x) = \partial_\mu B_\nu(t,x) - \partial_\nu B_\mu(t,x) + [B_\mu(t,x), B_\nu(t,x)], \tag{3.3}$$

where A_μ is the fundamental gauge field in pure SU(N_c) gauge theory, B_μ is the deformed gauge field characterized by the flow time t, and $G_{\mu\nu}$ is the field strength composed by B_μ, respectively. Note that the flow time t has the mass dimension -2. The right hand side of Eq. (3.1) is proportional to the gradient of the gauge action for B_μ, so that the solution for the equation is towards the stationary point of the gauge action. At the flow time $t > 0$, the deformed gauge field is smeared over the range $\sqrt{8t}$. Thus, we can consider B_μ as the renormalized field with the typical energy scale $\sqrt{t}$. Moreover, in Ref. [43], it is shown that the gauge-invariant local operators composed by B_μ are independent of the gauge fixing parameter in the gradient flow equation, and they become the UV finite for $t > 0$.

3.1.1 Energy density

One of the simple gauge-invariant operators is the energy density

$$E(t,x) = \frac{1}{4} G^a_{\mu\nu}(t,x) G^a_{\mu\nu}(t,x), \tag{3.4}$$

and in Ref. [42] the one-loop order computation of E is written as

$$\langle E(t) \rangle = \frac{3(N_c^2-1)}{32\pi t^2} \alpha_s(\mu_R^2) \left[1 + k_1 \alpha_s(\mu_R^2) + \mathcal{O}(\alpha_s^3) \right], \tag{3.5}$$

$$k_1 = \frac{1}{4\pi} N \left(\frac{11}{3} \gamma_E + \frac{52}{9} - 3 \log 3 \right), \tag{3.6}$$

where γ_E is the Euler's constant, and α_s is the running coupling at the scale μ_R with the renormalized coupling g in the $\overline{\rm MS}$ scheme. The higher-order calculation of $\langle E(t)\rangle$ is shown in Ref. [65].

The four-loop β-function for pure SU(N_c) gauge theory is given by

$$\mu_R^2 \frac{d\alpha_s}{d\mu_R^2} = -\sum_{k=0}^{3} b_k \alpha_s^{k+2}, \tag{3.7}$$

where coefficients b_0, b_1, b_2 and b_3 are obtained in Ref. [66]:

$$\begin{aligned} b_0 &= \frac{1}{4\pi}\frac{11}{3}N_c, \quad b_1 = \frac{1}{(4\pi)^2}\frac{34}{3}N_c^2, \quad b_2 = \frac{1}{(4\pi)^3}\frac{2857}{54}N_c^3, \\ b_3 &= \frac{1}{(4\pi)^4}\left\{\left(\frac{150653}{486} - \frac{44}{9}\zeta_3\right)N_c^4 + \frac{N_c^2(N_c^2+36)}{24}\left(-\frac{80}{9} + \frac{704}{3}\zeta_3\right)\right\}, \end{aligned} \tag{3.8}$$

where ζ_n is the Riemann zeta-function and $\zeta_3 \sim 1.2020569$. It is well known that coefficients b_n ($n \geq 3$) depend on the renormalization scheme. The solution for the β-function (3.7) is given by

$$\begin{aligned} \alpha_s(\mu_R^2) \sim \frac{1}{b_0\tilde{t}}\Bigg\{1 - \frac{b_1}{b_0}\frac{\log\tilde{t}}{\tilde{t}} + \frac{b_1^2\left(\log^2\tilde{t} - \log\tilde{t} - 1\right) + b_0 b_2}{b_0^2\tilde{t}^2} \\ - \frac{b_1^3\left(\log^3\tilde{t} - \frac{5}{2}\log^2\tilde{t} - 2\log\tilde{t} + \frac{1}{2}\right) + 3b_0 b_1 b_2 \log\tilde{t} - \frac{1}{2}b_0^2 b_3}{b_0^6\tilde{t}^3}\Bigg\}, \end{aligned} \tag{3.9}$$

where $\tilde{t} \equiv \log(\mu_R^2/\Lambda_{\overline{\rm MS}}^2)$, $\mu_R^2 = 1/8t$, and Λ is the momentum cutoff parameter in the $\overline{\rm MS}$ scheme.

In the lattice gauge theory, a reference scale gives the relation between the lattice coupling constant and the lattice spacing. In Ref. [42], a new reference scale by using $E(t,x)$ is proposed:

$$t^2\langle E(t)\rangle|_{t=t_0} = A, \tag{3.10}$$

where $t^2\langle E(t)\rangle$ is a dimensionless quantity. One of advantages using this scale is that the statistical uncertainty is smaller than that of other reference scales, since $E(t,x)$ is a local operator. In Ref. [42], the reference scale for pure SU(3) gauge theory is set to $A = 0.3$, and this gives almost the same reference scale as the Sommer scale [67]. This reference scale is suitable to study the thermodynamics around the critical temperature T_c.

3.1.2 Energy-momentum tensor

The energy-momentum tensor (EMT) $T_{\mu\nu}(x)$ for pure SU(N_c) gauge theory in the continuum spacetime is derived by

$$T_{\mu\nu}(x) = \frac{1}{g^2}\left[F^a_{\mu\rho}(x)F^a_{\nu\rho}(x) - \frac{1}{4}\delta_{\mu\nu}F^a_{\rho\sigma}(x)F^a_{\rho\sigma}(x)\right]. \tag{3.11}$$

In general, computing the EMT on the lattice is difficult, since the translational symmetry is broken by the lattice regularization. In this study, we calculate the EMT by the technique proposed in Refs. [41, 43].

For the flow time $t > 0$, the EMT in the $4+1$ dimension is given by

$$U_{\mu\nu}(t,x) = G^a_{\mu\rho}(t,x)G^a_{\nu\rho}(t,x) - \frac{1}{4}\delta_{\mu\nu}G^a_{\rho\sigma}(t,x)G^a_{\rho\sigma}(t,x). \tag{3.12}$$

As mentioned above, this operator and the energy density (3.4) are UV finite in pure SU(N_c) gauge theory. For the small flow time, they can be expanded by

$$U_{\mu\nu}(t,x) = \alpha_U(t)\left\{T^R_{\mu\nu}(x) - \frac{1}{4}\delta_{\mu\nu}T^R_{\rho\rho}(x)\right\} + \mathcal{O}(t), \tag{3.13}$$

$$E(t,x) = \langle E(t,x)\rangle_0 + \alpha_E(t)T^R_{\rho\rho} + \mathcal{O}(t), \tag{3.14}$$

where $T^R_{\mu\nu}(x)$ is the renormalized EMT in the 4-dimensional space, and $\langle E(t,x)\rangle_0$ denotes the expectation value of the energy density $E(t,x)$ at zero temperature. Thus, $T^R_{\mu\nu}(x)$ is obtained as

$$T^R_{\mu\nu}(x) = \lim_{t\to 0}\left\{\frac{1}{\alpha_U(t)}U_{\mu\nu}(t,x) + \frac{\delta_{\mu\nu}}{4\alpha_E(t)}\left\{E(t,x) - \langle E(t,x)\rangle_0\right\} + \mathcal{O}(t)\right\}. \tag{3.15}$$

This is a conserved quantity, so that it must be independent of the renormalization scheme. Hence, coefficients $\alpha_U(t)$ and $\alpha_E(t)$ should be also independent of the scheme. However, it is difficult to evaluate them nonperturbatively. Here, we adopt the representation in the one-loop order shown in Ref. [41]:

$$\alpha_U(t) = 4\pi\alpha_s(\mu_R^2)\left\{1 + 2b_0\bar{s}_1\alpha_s(\mu_R^2) + \mathcal{O}\left(\alpha_s(\mu_R^2)^2\right)\right\}, \tag{3.16}$$

$$\alpha_E(t) = \frac{2\pi}{b_0}\left\{1 + 2b_0\bar{s}_2\alpha_s(\mu_R^2) + \mathcal{O}(\alpha_s(\mu_R^2)^2)\right\}. \tag{3.17}$$

The coefficients $\bar{s}_1$ and $\bar{s}_2$ depend on the renormalization scheme, and in the $\overline{\text{MS}}$ scheme they are given by

$$\bar{s}_1 = \frac{7}{22} + \frac{\gamma_E}{2} - \log 2 \sim -0.08635752993, \tag{3.18}$$

$$\bar{s}_2 = \frac{21}{44} - \frac{b_1}{2b_0^2} \sim 0.0557812397. \tag{3.19}$$

At finite temperature, we can measure the thermodynamic quantities by using $T^R_{\mu\nu}$ as following:

$$\Delta = \varepsilon - 3P = -\sum_{\mu=1}^{4} T^R_{\mu\mu}, \tag{3.20}$$

$$sT = \varepsilon + P = T^R_{11} - T^R_{44}, \tag{3.21}$$

where Δ, s, ε, and P represent the trace anomaly, the entropy density, the energy density, and the pressure, respectively.

3.1.3 Gradient flow on the lattice

The gradient flow equation on the lattice is given by [42]

$$\partial_t V_\mu(t,x) = -g_0^2 \left\{\partial_{x,\mu} S_W(V)\right\} V_\mu(t,x), \tag{3.22}$$

$$V_\mu(t=0,x) = U_\mu(x), \tag{3.23}$$

where U_μ is the link variable, V_μ is the deformed one, and S_W denotes the Wilson-plaquette action. The derivative operator for the function $f(U)$ ($U \in \mathrm{SU}(N_c)$) is given by

$$\partial_{x,\mu} f(U) = T^a \partial^a_{x,\mu} f(U), \quad \partial^a_{x,\mu} f(U) = \left.\frac{d}{ds} f(e^{sX} U)\right|_{s=0}, \tag{3.24}$$

$$X(y,\nu) = \begin{cases} T^a & \text{if } (y,\nu) = (x,\mu), \\ 0 & \text{otherwise.} \end{cases} \tag{3.25}$$

The equation (3.22) is the first-order differential equation, so we can solve it by using the third-order Runge-Kutta method. The formulation with the initial condition (3.23) is shown in Ref. [42]. The solution of Eq. (3.22) from t to $t+\epsilon$ is derived by

$$\begin{aligned} W_0 &= V_\mu(t,x), \\ W_1 &= \exp\left[\frac{1}{4} Z_0\right] W_0, \\ W_2 &= \exp\left[\frac{8}{9} Z_1 - \frac{17}{36} Z_0\right] W_1, \\ V_\mu(t+\epsilon,x) &= \exp\left[\frac{3}{4} Z_0 - \frac{8}{9} Z_1 + \frac{17}{36} Z_0\right] W_2, \end{aligned} \tag{3.26}$$

$$Z_i = \epsilon Z(W_i), \quad Z(W_i) = -g_0^2 \left\{\partial_{x,\mu} S_W(W_i)\right\}. \tag{3.27}$$

In this study, we take $\epsilon/a^2 = 0.01$.

3.2 Simulation setup

In our lattice simulation, we use the standard Wilson-Plaquette action

$$S_W = \beta \sum_{x,\mu>\nu} \left\{1 - \frac{1}{N} \mathrm{tr} U_{\mu\nu}(x)\right\}, \tag{3.28}$$

$$U_{\mu\nu}(x) = U_\mu(x) U_\nu(x+\hat{\mu}) U^\dagger_\mu(x+\hat{\nu}) U^\dagger_\nu(x), \tag{3.29}$$

where β is the lattice coupling constant defined by $\beta = 2N_c/g_0^2$. For U_μ, we take the periodic boundary condition.

When updating configurations, we use one pseudo-heatbath step with the multiple over-relaxation steps. The ratio of the combination is $1:20$ for $T=0$, and $1:N_\tau$ for $T=(aN_\tau)^{-1}$. To avoid the autocorrelation, we

take 100 sweeps between measurements. In this study, we take 100 $\sim$ 600 configurations to measure observables, and set the lattice extent $N_s^4 = 32^4$ for the zero temperature simulation, while we take 200 configurations on the lattice extents $N_s^3 \times N_\tau = 24^3 \times 6$, $32^3 \times 8$, $40^3 \times 10$, and $48^3 \times 12$ for the finite temperature one.

3.3 Scale setting

In order to obtain the relation between the lattice coupling constant β and the lattice spacing a, we do the scale setting with the t_0-scale as the reference scale. In the previous study, the t_0-scale for pure SU(3) gauge theory is set to $A = 0.3$ in Ref. [42]. Similar scales for pure SU(2) gauge theory are also proposed in Ref. [68]. In this study, we set the reference value for pure SU(2) gauge theory to

$$A = t^2 \langle E(t) \rangle \big|_{t=t_0} = 0.1. \tag{3.30}$$

This is the approximated scaling-down value from that for pure SU(3) gauge theory, since $\langle E(t) \rangle$ in the perturbative analysis is proportional to the factor $(N_c^2 - 1)$.

When measuring the energy density $E(t, x)$, we use the following two definitions:

$$\text{Plaquette definition: } E(t,x) = 2 \sum_{\mu > \nu} \text{Re tr} \left[1 - P_{\mu\nu}(t,x) \right], \tag{3.31}$$

$$\text{Clover-leaf definition: } E(t,x) = -\frac{1}{2} \sum_{\mu,\nu} \text{tr} \left[\tilde{G}_{\mu\nu}(t,x) \tilde{G}_{\mu\nu}(t,x) \right], \tag{3.32}$$

where $P_{\mu\nu}(t, x)$ denotes the plaquette composed by the deformed link variable $V_\mu(t, x)$ at the finite t, and $\tilde{G}_{\mu\nu}(t, x)$ is an improved deformed field strength given by [69, 70]

$$\tilde{G}_{\mu\nu}(t,x) = \frac{1}{4} \left\{ P_{\mu\nu}(t,x) + Q_{\mu\nu}(t,x) + R_{\mu\nu}(t,x) + S_{\mu\nu}(t,x) \right\}, \tag{3.33}$$

$$Q_{\mu\nu}(t,x) = V_\nu^\dagger(t, x - \hat{\nu}) V_\mu(t, x - \hat{\nu}) V_\nu(t, x + \hat{\mu} - \hat{\nu}) V_\mu^\dagger(t,x) \tag{3.34}$$

$$R_{\mu\nu}(t,x) = V_\mu^\dagger(t, x - \hat{\mu}) V_\nu^\dagger(t, x - \hat{\mu} - \hat{\nu}) V_\mu(t, x - \hat{\mu} - \hat{\nu}) V_\nu(t, x - \hat{\nu}) \tag{3.35}$$

$$S_{\mu\nu}(t,x) = V_\nu(t,x) V_\mu^\dagger(t, x - \hat{\mu} + \hat{\nu}) V_\nu^\dagger(t, x - \hat{\mu}) V_\mu(t, x - \hat{\mu}), \tag{3.36}$$

respectively. In the continuum limit, the results obtained by using both the definitions should be same.

Before the scale-setting simulation, we need to compare the behavior of $t^2 \langle E(t) \rangle$ of the perturbative result and the lattice result. To see them, we take $\beta = 2.85$.

In Ref. [71], the renormalized coupling g_{SF} in the Schrödinger functional (SF) scheme for pure SU(2) gauge theory was studied, and the β-function is

given by

$$L\frac{\partial g_{\rm SF}}{\partial L} = g_{\rm SF}^3\left\{\frac{b_0}{4\pi} + \frac{b_1}{(4\pi)^2}g_{\rm SF}^2 + \frac{b_2^{\rm eff}}{(4\pi)^4}g_{\rm SF}^4\right\}, \tag{3.37}$$

$$b_2^{\rm eff} = 0.35(12), \tag{3.38}$$

where L is the box size, and $b_2^{\rm eff}$ is the effective coefficient given in Ref. [71]. When choosing the condition $g_{\rm SF}^2(L_0^{\rm SF}) = 4.765$, we can calculate $L_0^{\rm SF}\Lambda_{\rm SF}$:

$$L_0^{\rm SF}\Lambda_{\rm SF} = 0.1804^{+0.0101}_{-0.0064}. \tag{3.39}$$

At $\beta = 2.85$, by using the tree-level action in the SF scheme, we can obtain the ratio of the lattice spacing a to $L_0^{\rm SF}$ as $a/L_0^{\rm SF} = 0.0843(5)$. The ratio of Λ parameter between the SF and the $\overline{\rm MS}$ schemes is given by $\Lambda_{\rm SF}/\Lambda_{\overline{\rm MS}} = 0.44567$ in Ref. [71]. Thus, we obtain $\Lambda_{\overline{\rm MS}}$ in the lattice unit at $\beta = 2.85$ as

$$a\Lambda_{\overline{\rm MS}} = 0.0338^{+0.0021}_{-0.0014}. \tag{3.40}$$

Figure 3.1 shows the result of $t^2\langle E(t)\rangle$ at $\beta = 2.85$, where the lattice result is calculated by using the clover-leaf definition. The solid curve represents the result of the perturbative calculation using Eqs. (3.5) with the parameter (3.40), while the band shows the lattice result with the statistical error. It is seen that both the perturbative and lattice results are consistent within the statistical error for the small flow time.

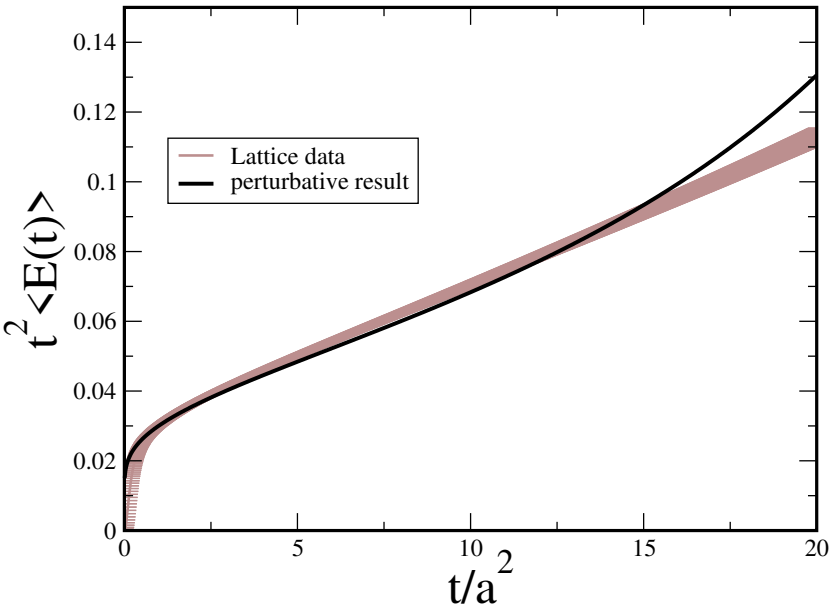

Figure 3.1: Comparison of $t^2\langle E(t)\rangle$ between the lattice result and the perturbative calculation at $\beta = 2.85$.

3.3.1 t_0-scale for pure SU(2) gauge theory

For the scale-setting simulation, we measure $t^2\langle E(t)\rangle$ by using both the plaquette and clover-leaf definitions. When solving the gradient flow equation (3.1), we set $t/a^2 \in [0.00, 32.00]$ as a range of the flow time.

Figure 3.2 shows the results of the t/a^2-dependence of $t^2 \langle E(t) \rangle$ with both the plaquette and clover-leaf definitions at $\beta = 2.500$, 2.700 and 2.850. In Ref. [42], the results of pure SU(3) gauge theory show that $t^2 \langle E(t) \rangle$ has a linear behavior in the large flow time region. In Fig. 3.2, it is also seen that our results of pure SU(2) gauge theory have the same behavior. On the other hand, in the small flow time region, $t^2 \langle E(t) \rangle$ with the plaquette definition rapidly increases. This behavior may comes from the lattice discretization effect. Therefore, we mainly use the clover-leaf definition for the scale setting.

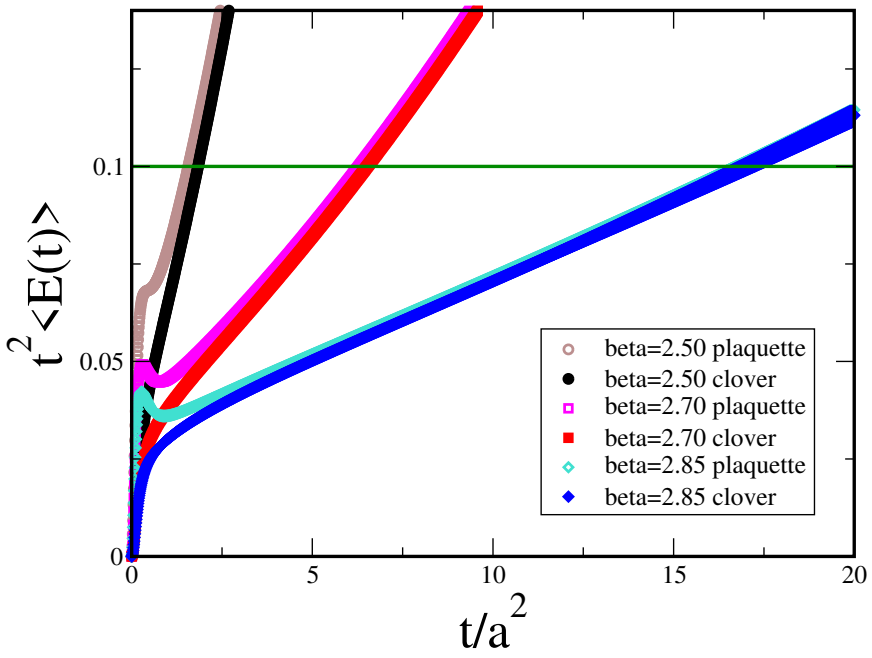

Figure 3.2: t/a^2-dependence of $t^2 \langle E(t) \rangle$ with both the plaquette and clover-leaf definitions at $\beta = 2.500$, 2.700 and 2.850. The open symbols represents the results with the plaquette definition, and the filled ones denotes the results with the clover-leaf definition.

Table 3.1 shows the number of configurations to measure the observable for each β and the results of t_0/a^2. At $\beta = 2.400$, t_0/a^2 is smaller than 1. In order to avoid the lattice discretization effect, we drop this data. To avoid a finite-volume effect, we need to consider the region $\sqrt{8t/a^2} \leq 32/2$, since all link variables are smeared in $\sqrt{8t/a^2} > 32/2$. The calculation of the data at $\beta = 2.900$ is also carried out in our study, but $t^2 \langle E(t) \rangle$ does not increase larger than the reference value. Thus, we do not consider the data at $\beta = 2.900$. By using the results of t_0/a^2 for $\beta \in [2.420, 2.850]$, we obtain the best fit function for $\log(t_0/a^2)$ as

$$\log(t_0/a^2) = 1.258 + 6.409(\beta - 2.600) - 0.7411(\beta - 2.600)^2, \qquad (3.41)$$

In Fig. 3.3, the ratio of the lattice spacing $\log(a^2/a_0^2)$ is shown, where we set a_0 to the value at $\beta = 2.500$. We also plot the result of the scale-setting function obtained in Ref. [49], where this function is available in

Table 3.1: Simulation setup for each β. The results of t_0/a^2 are also summarized.

β	# of Conf.	t_0/a^2
2.400	300	0.9549(5)
2.420	100	1.083(2)
2.500	300	1.839(3)
2.600	300	3.522(10)
2.700	300	6.628(36)
2.800	300	11.96(12)
2.850	600	16.95(17)

$2.42 \leq \beta \leq 2.60$ and suitable to study the physics in $T \leq T_c$. The error bar is estimated by using the covariance matrix of the chi-square fit. It is seen that both the results are consistent within the error bar where both the functions are available, and our result is more precise than that shown in Ref. [49]. Moreover, our scale-setting function covers the higher β, so that we can investigate the physics in $T \geq T_c$ with our function.

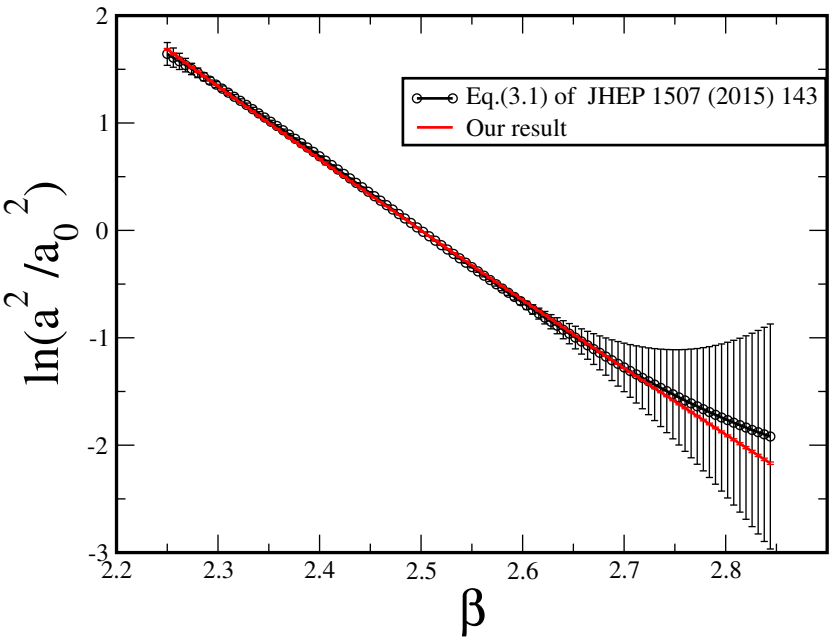

Figure 3.3: Ratio of the lattice spacing $\log(a^2/a_0^2)$, where a_0 is set to the value at $\beta = 2.500$. The red data is the scale-setting function given in Eq. (3.41), and the black one is the result shown in Ref. [49].

3.3.2 Relation between t_0- and other reference scales

To study the relation between t_0-scale and other reference scales, we compare our scale $\sqrt{8t_0}$ with the Sommer scale (r_0-scale) [67] and the Necco-Sommer

scale (r_c-scale) [72]. These reference scales are defined via the static quark-antiquark force $F(r)$: the r_0-scale (r_c-scale) is determined by $r^2F(r)|_{r=r_0} = 1.65$ ($r^2F(r)|_{r=r_c} = 0.65$).

Figure 3.4 shows the continuum extrapolation of the ratio of $\sqrt{8t_0}$ and r_0 or r_c. Here, we estimate values r_0/a and r_c/a by using the data at $\beta = 2.50$, 2.60, and 2.70 shown in Ref. [67]. In both the panels, the filled square and the open circle symbols represent the results calculated by using both the clover-leaf and the plaquette definitions for the operator $E(t, x)$, respectively. The results obtained by the clover-leaf definition have the gentle slope, and it is indicated that the discretization error is much smaller than that of data calculated by the plaquette definition. In both the panels of Fig. 3.4, it is also seen that the continuum extrapolated results by using both the definitions agree with each other.

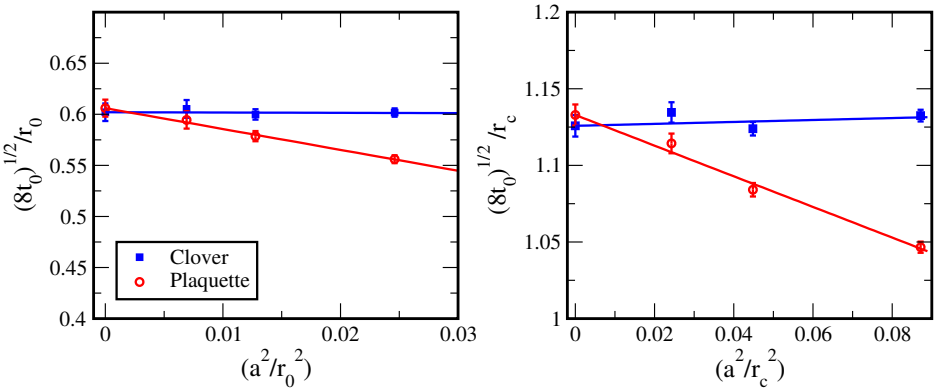

Figure 3.4: Continuum extrapolation of ratios of $\sqrt{8t_0}$ and r_0 (left) or r_c (right). The filled square symbol denotes the result by using the clover-leaf definition, while the open circle one does that by using the plaquette definition.

The continuum extrapolated values of ratios $\sqrt{8t_0}/r_0$ and $\sqrt{8t_0}/r_c$ with the clover-leaf definition are

$$\frac{\sqrt{8t_0}}{r_0} = 0.6020(86)(40), \quad \frac{\sqrt{8t_0}}{r_c} = 1.126(7)(7), \tag{3.42}$$

where the first bracket represents the statistical error, and the second one shows the systematic error estimated by the difference from the value evaluated with the plaquette definition. From these results, we can conclude that our t_0-scale for pure SU(2) gauge theory is similar to the r_c-scale rather than the r_0-scale, while the t_0-scale for pure SU(3) gauge theory is closer to the r_0-scale. In Ref. [67], the r_0-scale is taken to $r_0 = 0.5$ [fm], and our scale $\sqrt{8t_0}$ is estimated as $\sqrt{8t_0} = 0.3010(43)(20)$ [fm] in the physical unit.

For a consistency check of our results, we consider σr_0^2, where σ denotes the string tension. To evaluate σr_0^2, we use the data of $a^2\sigma$ given in Refs. [49, 73], and t_0/a^2 obtained with the clover-leaf definition. Figure 3.5 shows the results of $8t_0\sigma$ and the continuum extrapolated ones. The square data

are calculated with $a\sigma^2$ at $\beta = 2.42$, 2.50 and 2.60 given in Ref. [49], and the continuum extrapolated value is $8t_0\sigma = 0.484(11)$. On the other hand, the circle symbols denote the results evaluated with $a^2\sigma$ at $\beta = 2.50$, 2.60, 2.70, and 2.85 shown in Ref. [73], and the data becomes $8t_0\sigma = 0.546(11)$ in the continuum limit. The difference between them is 6 times the statistical error, and it mainly comes from the difference of the data $a\sigma^2$ at $\beta = 2.50$ between Refs. [49] and [73]. By using values of $8t_0\sigma$, we get $\sigma r_0^2 = 1.34(7)$ for the former data, and $\sigma r_0^2 = 1.51(8)$ for the latter data. These results are consistent within the statistical error bar of the result $\sigma r_0^2 = 1.39(50)$ shown in Ref. [67].

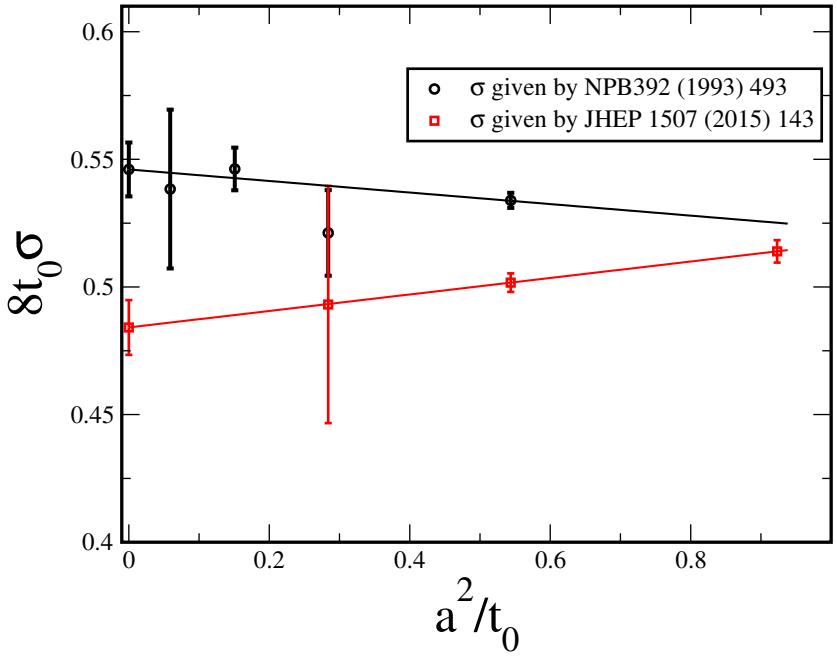

Figure 3.5: Continuum extrapolated $8t_0\sigma$. The square symbol represents the result calculated with $a^2\sigma$ given in Ref. [49], while the data $a^2\sigma$ for the circle symbol is shown in Ref. [73].

In Ref. [73], $T_c/\sqrt{\sigma} = 0.69(2)$, $T_c/\Lambda_{\overline{\rm MS}} = 1.23(11)$, and $\sqrt{\sigma}/\Lambda_{\overline{\rm MS}} = 1.79(12)$ are given. Thus, by using the value $8t_0\sigma = 0.484(11)$, we can obtain the relation between our t_0-scale and the critical temperature T_c or the renormalization scale in the $\overline{\rm MS}$ scheme for pure SU(2) gauge theory:

$$\sqrt{8t_0}T_c = 0.480(20), \quad \sqrt{8t_0}\Lambda_{\overline{\rm MS}} = 0.389^{+0.032}_{-0.029}. \tag{3.43}$$

From these results, $T_c < 1/\sqrt{8t_0} \sim 2T_c$, so that our scale is suitable for investigating the physics in $T_c \lesssim T \lesssim 2T_c$.

3.4 Thermodynamics

By using the scale-setting function (3.41), we can obtain the relation between the lattice coupling β and temperature $T = (N_\tau a)^{-1}$. To do this, we fix

$\beta = 2.4265$ for the critical temperature T_c with $N_\tau = 6$ shown in Ref. [47]. The estimated β for T/T_c with each N_τ are shown in Table. 3.2, and we obtain the estimated β for $T/T_c = 1$ with $N_\tau = 8$, 10, and 12 as $\beta = 2.514$, 2.583, and 2.650, respectively. In the previous study [74], the critical values of β obtained by using the Polyakov loop susceptibility are $\beta = 2.510363(71)$, 2.57826(14), and 2.63625(35) for $N_\tau = 8$, 10, and 12. By comparing the estimated values with them, our values are consistent within the two- or three-digit accuracy. In this study, we use estimated values of β in the three-digit accuracy for the finite temperature simulation. In Tab. 3.2, the values of β in the bracket are outside of the range for the scale-setting function (3.41), so that we exclude these data in our analysis.

Table 3.2: Parameter sets for the finite temperature simulation

T/T_c	$N_\tau = 6$	$N_\tau = 8$	$N_\tau = 10$	$N_\tau = 12$
0.95	(2.41)	2.50	2.57	2.62
0.98	2.42	2.51	2.58	2.63
1.01	2.43	2.52	2.59	2.64
1.04	2.44	2.53	2.60	2.65
1.08	2.45	2.54	2.61	2.66
1.12	2.46	2.55	2.62	2.67
1.28	2.50	2.59	2.66	2.72
1.50	2.55	2.64	2.71	2.77
1.76	2.60	2.69	2.76	2.82
2.07	2.65	2.74	2.81	(2.87)

3.4.1 Numerical results

To obtain the renormalized EMT on the lattice, we use the clover-leaf definition to construct operators, and follow the procedures shown in Ref. [44]:

1. Generate gauge configurations at $t = 0$ on the lattice $N_s^3 \times N_\tau$ with the lattice spacing a.

2. Solve the gradient flow equation (3.22) to obtain the deformed link variables in the fiducial window $a \ll \sqrt{8t} \ll R$ to reduce the finite volume and the discretization effects. R is the infrared cutoff parameter such as $\Lambda_{\rm QCD}^{-1}$ or $N_\tau a$.

3. Construct the operators $E(t, x)$ and $U_{\mu\nu}(t, x)$ shown in Eqs. (3.4) and (3.12), and take the configuration average at each t.

4. Carry out an extrapolation $(a, t) \to (0, 0)$, first $a \to 0$ and then $t \to 0$ in the fiducial window.

The lower limit of the fiducial window is related to the discretization effect, while the upper one is related to the smearing effect by the gradient flow. In this study, we set the lower limit to $\sqrt{8t_{\rm min}} = 2a$, since we use the clover-leaf definition with a size $2a$. On the other hand, we fix $\sqrt{8t_{\rm max}} = 0.35N_\tau$ proposed in Ref. [75], since the smearing effect doesn't exceed the temporal lattice size $N_\tau a$. Thus, the fiducial window in this study becomes $2/N_\tau \leq \sqrt{8t}T \leq 0.35$.

When carrying out both the extrapolation $(a, t) \to (0, 0)$, we need to estimate the error propagation carefully, since the deformed data by the gradient flow after the continuum limit is correlated with other data. Here, we use the jackknife method: firstly generate the jackknife samples for the data E and $U_{\mu\nu}$ at each t, secondly obtain the renormalized EMT by taking the double extrapolations for the samples, and finally calculate the standard error.

Figure 3.6 shows the flow time dependence of the dimensionless trace anomaly Δ/T^4 (top two panels) and the dimensionless entropy density s/T^3 (bottom two panels). The left two panels represent the N_τ-dependence at $T/T_c = 1.12$, while the right two ones show the temperature dependence with $N_\tau = 12$. Here, the error bar shows the statistical uncertainty, and the dashed (dotted) line denotes the lower (upper) limit of the fiducial window for each N_τ. In all panels of Fig. 3.6, it is seen that the data with the statistical error for each N_τ or T have the plateau behavior in the fiducial window.

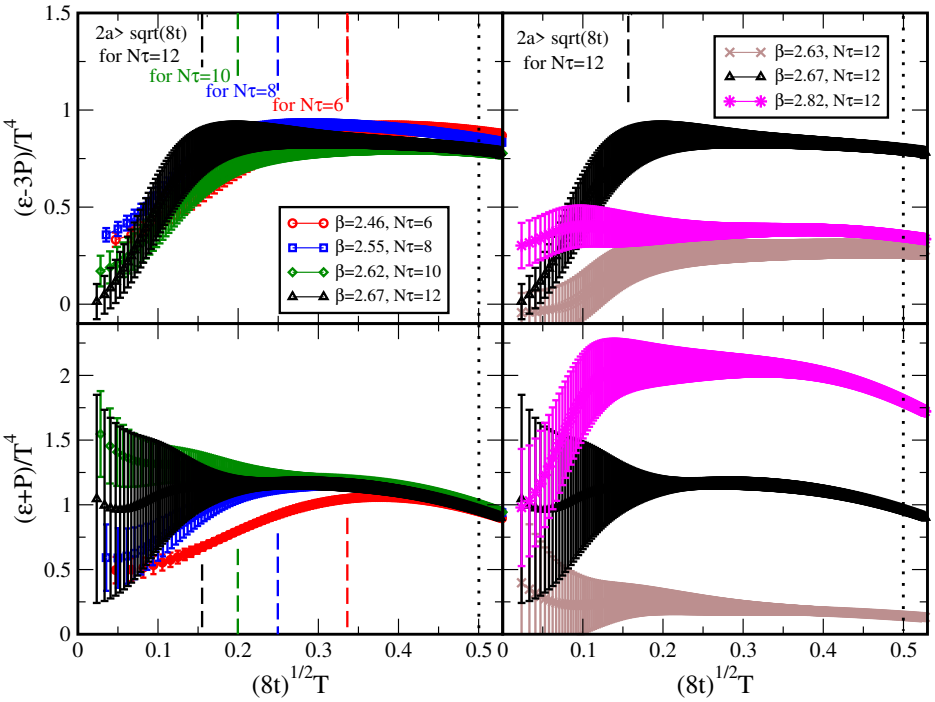

Figure 3.6: Flow time dependence of Δ/T^4 (upper two panels) and s/T^3 (lower two panels). Left two panels show the N_τ-dependence at $T/T_c = 1.12$, while right two ones do the temperature dependence with $N_\tau = 12$.

When taking double limits $(a, t) \to (0, 0)$, we use both the constant and linear extrapolations for datasets: 16 fixed flow time $\sqrt{8t}T \in [0.25, 0.35]$ with $\delta(\sqrt{8t}T) = 0.01$ for each temperature T/T_c summarized in Tab. 3.2. In the continuum limit, we carry out the constant extrapolation to obtain the central values, and the linear one to estimate the systematic error. For the constant extrapolation, we use data with $N_\tau = 8$, 10, and 12 in $0.95 \leq T/T_c \leq 1.76$ in order to exclude the discretization error coming from the data with $N_\tau = 6$. On the other hand, at $T/T_c = 2.07$, we cannot use data with $N_\tau = 12$, and the discretization error of data with $N_\tau = 6$ is considered to be small in $\sqrt{8t}T > 1/3$. Thus, we use two data ($N_\tau = 8$ and 10) in $\sqrt{8t}T < 1/3$ and three data ($N_\tau = 6$, 8, and 10) in $\sqrt{8t}T > 1/3$ at $T/T_c = 2.07$. For the linear extrapolation, we use all data points which we can use.

Figure 3.7 shows the plot of the continuum extrapolations at $T/T_c = 0.98$, 1.08, and 1.76. The solid and dashed lines represent the constant and linear extrapolations of $(Ta)^2 = 1/N_\tau^2$, respectively. After taking the continuum limit, both the fitted values of the trace anomaly (entropy density) are consistent within 2 times (3 times) the statistical error.

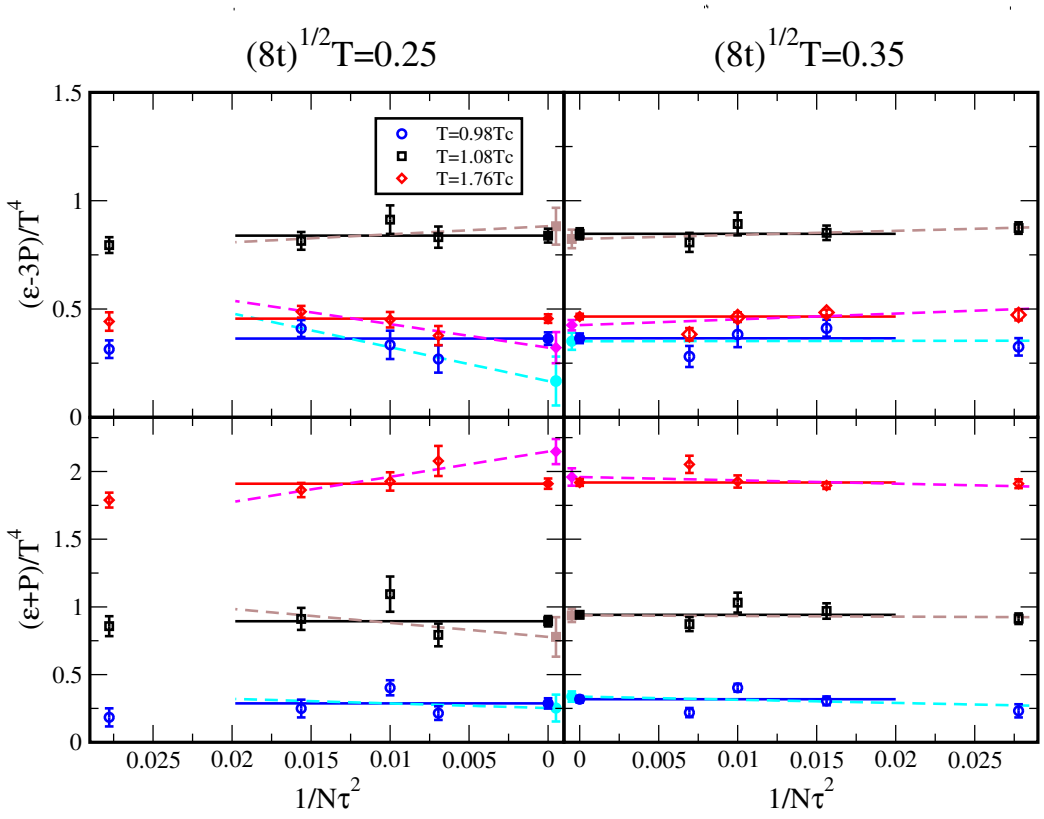

Figure 3.7: Extrapolation of $a \to 0$ for the fixed flow time $\sqrt{8t}T = 0.25$ and 0.35. The solid and dashed lines show the constant and linear extrapolation, respectively.

Figure 3.8 shows the extrapolation $t \to 0$. The solid and dashed lines represent the constant and the linear extrapolations of $8tT^2$. For the central

value, we use the fitted value with the better reduced χ^2, and estimate the systematic uncertainty from the difference between the value and the other extrapolated one. Both the values for the trace anomaly (entropy density) are consistent within the statistical error (3 times the statistical error).

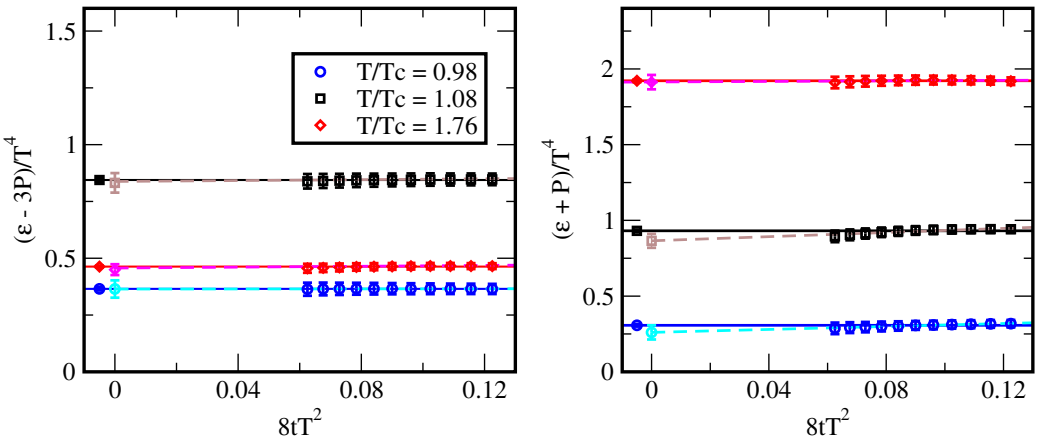

Figure 3.8: Extrapolation of $t \to 0$ for $T/T_c = 0.98$, 1.08, and 1.76, respectively. The solid and dashed lines show the constant and linear extrapolation, respectively.

The dimensionless parameter $a\Lambda_{\overline{\rm MS}}$ has errors. Thus, we also estimate the systematic error from it. The error affects the values of the coefficients α_U and α_E via the renormalized coupling g, and the effects are expected to become large at low temperature since the running coupling α_s glows up rapidly as temperature decreases. The estimated systematic error for the trace anomaly is much smaller than the statistical error, while that for the entropy density has 6% of the central value.

In the left panel of Fig. 3.9, we plot the results of the trace anomaly (circle symbol) and the entropy density (cube symbol) after taking the double limits $(a, t) \to (0, 0)$. The statistical errors are shown by the error bars. The results by using the integral method with the improved action with $N_\tau = 5$ [68] (triangle symbol: trace anomaly, diamond symbol: entropy density) are also shown. In $T/T_c \geq 1.12$, both the results are consistent within the errors including all systematic errors. On the other hand, in $T/T_c < 1.12$, it is seen that our results are little larger than the results given in Ref. [68]. This discrepancy may come from the following two results: one is the discretization error of the results given in Ref. [68], and the other is the usage of the one-loop order coefficients when calculating the renormalized EMT.

The right panel of Fig. 3.9 shows the result of the equation of state (EOS) in $T \geq T_c$. The EOS represents the relation between the energy density ε and the pressure P. The dashed line denotes the linear function $P = \varepsilon/3$ in the case of $\Delta/T^4 = 0$, and the diamond symbol shows the values in the Stefan-Boltzmann (SB) limit. In the high temperature region ($T/T_c \gtrsim 1.50$), our data is approaching to the values in the SB limit. However, at $T \sim 2T_c$,

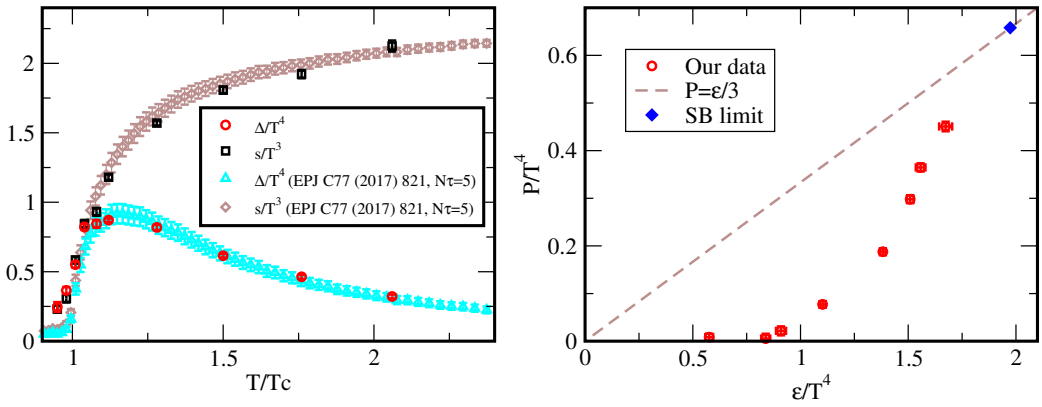

Figure 3.9: Results of (left) the entropy density, trace anomaly, and (right) EOS, respectively. In the left panel, we also plot the results of the entropy density (diamond symbol) and trace anomaly (triangle symbol) obtained in Ref. [68]. In the right panel, the diamond symbol denotes the Stefan-Boltzmann limit $(\varepsilon/T^4, P/T^4) = (\pi^2/5, \pi^2/15)$, and the dashed line does the case with $\Delta/T^4 = 0$.

our data has $70 \sim 85\%$ of the values in the limit. This result indicates that 2-color QGP around $T/T_c \leq 2$ cannot be described by the ideal gas model. The values of our results are summarized in Tab. 3.3.

Table 3.3: Results of thermodynamic quantities: trace anomaly Δ/T^4, entropy density s/T^3, energy density ε/T^4, and pressure P/T^4. The errors denote the statistical uncertainties.

T/T_c	Δ/T^4	s/T^3	ε/T^4	P/T^4
0.95	0.246(35)	0.232(27)	0.235(24)	-0.00348(1041)
0.98	0.365(25)	0.307(29)	0.322(24)	-0.0145(87)
1.01	0.551(22)	0.585(22)	0.576(18)	0.00848(739)
1.04	0.822(22)	0.844(29)	0.838(21)	0.00543(1019)
1.08	0.844(28)	0.931(28)	0.909(23)	0.0217(93)
1.12	0.871(13)	1.18(2)	1.10(1)	0.772(69)
1.28	0.819(20)	1.57(2)	1.38(1)	0.188(7)
1.50	0.615(13)	1.81(2)	1.51(2)	0.298(8)
1.76	0.463(14)	1.92(3)	1.56(2)	0.365(9)
2.07	0.322(14)	2.12(4)	1.67(3)	0.451(10)

Next, we compare our results with the prediction of the Hard-Thermal-Loop (HTL) model [34] with the next-to-next-to-leading order (NNLO) representation in the 2-color case. Figure 3.10 shows the comparison between our data and the prediction of the HTL model. In both the panels, the solid line denotes the result of the HTL model with the renormalization parameter $\mu_{\rm HTL}/(2\pi T) = 1.0$, while the upper (lower) dashed line shows the result with $\mu_{\rm HTL}/(2\pi T) = 1.5$ (0.5), respectively. The band also represents

the systematic uncertainty from the parameter $T_c/\Lambda_{\overline{\rm MS}} = 1.23(11)$. For the energy density rescaled by the value in the SB limit, shown in the left panel of Fig. 3.10, it is seen that our result is consistent with the prediction of the HTL model in $T \gtrsim T_c$.

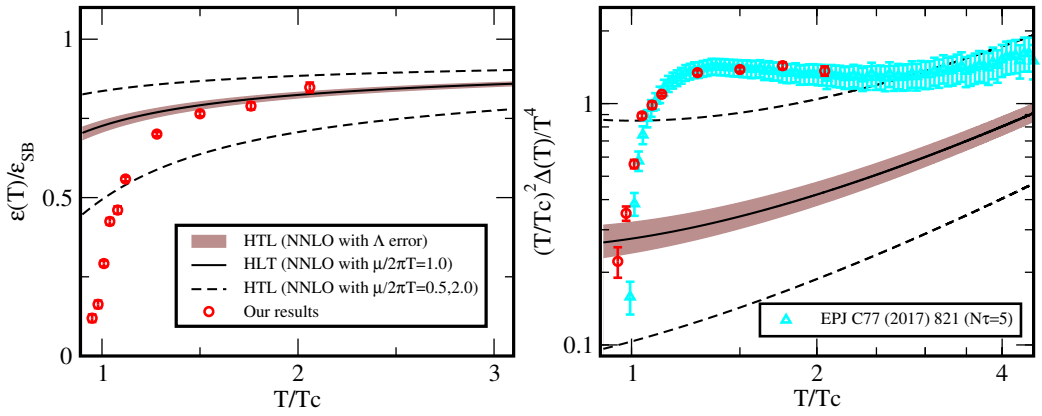

Figure 3.10: Comparison with the prediction of the HTL model. For the HTL model, we use the NNLO notation in the 2-color case shown in Ref. [34]. The left panel shows the result of the entropy density rescaled by that in the SB limit, while the right panel does the results of the rescaled trace anomaly. In both the panel, the solid line shows the result of HTL model with the renormalization scheme $\mu_{\rm HTL}/(2\pi T) = 1.0$, while the upper (lower) dashed line does that with $\mu_{\rm HTL}/(2\pi T) = 1.5$ (0.5), respectively. The band also represents the systematic uncertainty from $T_c/\Lambda_{\overline{\rm MS}} = 1.23(11)$. In the right panel, we also plot the result obtained in Ref. [68] as the triangle symbol.

In the right panel of Fig. 3.10, we plot the rescaled trace anomaly to see the scaling property. The data obtained in Ref. [68] is also shown. In the high temperature region, the trace anomaly is well fitted with the linear function of $1/T^2$ in $(T_c/T)^2 \lesssim 0.9$ for pure SU($N_c \geq 3$) gauge theory, shown in Ref. [48]. In $T/T_c \gtrsim 1.3$, the lattice results of pure SU(2) gauge theory have the plateau behavior, and are approaching to the HTL results. In pure SU(3) gauge theory [76], the trace anomaly has almost the same behavior as in pure SU(2) gauge theory, and becomes consistent with the prediction of the HTL model. Thus, it is expected that the lattice data in pure SU(2) gauge theory has the same behavior in $T/T_c \gtrsim 2$.

Finally, we compare the trace anomaly of pure SU(2) gauge theory with that of pure SU($N_c \geq 3$) gauge theories. Here, we use rescaled trace anomaly $(\Delta/T^4)/(P_{\rm SB}/T^4)$ as a function of $(T_c/T)^2$, where $P_{\rm SB}$ denotes the pressure in the SB limit. In Fig. 3.11, we plot our result and data obtained in Ref. [68] as the circle and triangle symbols, respectively. We also show the well-fitted linear functions for pure SU($3 \leq N_c \leq 8$) gauge theories given in Ref. [48]. For pure SU(2) gauge theory, both results have the curved behavior in $(T_c/T)^2 \gtrsim 0.6$, and the linear behavior in $(T_c/T)^2 \lesssim 0.6$. On the other hand, the rescaled trace anomaly for pure SU($3 \leq N_c \leq 8$) gauge theories

are well fitted with the linear function in $(T_c/T)^2 \leq 0.9$. We consider that the difference between them occurs due to the difference of the order of the phase transition.

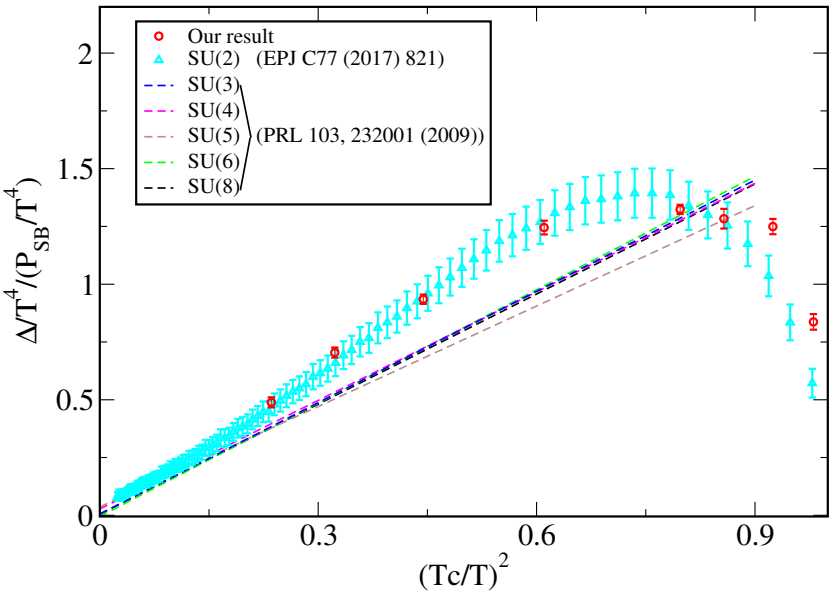

Figure 3.11: N_c-dependence of the rescaled trace anomaly $(\Delta/T^4)/(P_{\rm SB}/T^4)$. The circle and triangle symbols denote our data and the results obtained in Ref. [68], respectively. The several dashed lines show the well-fitted linear functions for pure SU($3 \leq N_c \leq 8$) gauge theories shown in Ref. [48].

3.5 Short summary

In this study, we determine the scale-setting function and obtain the thermodynamic quantities of pure SU(2) gauge theory by using the gradient flow.

For the scale setting, we propose the reference value $t^2 \langle E(t) \rangle |_{t=t_0} = 0.1$ for pure SU(2) gauge theory. The result shows that the statistical error is smaller than that given in [49], and our function is suitable to investigate the thermodynamics in $T_c \lesssim T \lesssim 2T_c$.

For the thermodynamic quantities of pure SU(2) gauge theory, we use the small flow-time expansion method to construct the renormalized EMT, and measure the thermodynamic quantities in the continuum limit. By comparing our results with that obtained by the integral method [68], our data are consistent especially in $T \gtrsim T_c$, and the statistical error is smaller even with less configurations. On the other hand, around T_c, our results are different from that obtained in Ref. [68]. It is considered that this discrepancy comes from the discretization error of the previous study and the usage of the one-loop coefficients for the renormalized EMT. Recently, in Ref. [65], the higher-order coefficients of the EMT was calculated, and the work in [77]

has showed that the systematic error is reduced by using the higher-order coefficients and the results are consistent with Refs. [33, 76, 78–80]. Therefore, by using the higher-order coefficients, it is expected that we can measure the thermodynamic quantities more precisely and improve the results around T_c.

In the high temperature region, we find the tendency which our results are approaching to the HTL predictions. For the energy density and the pressure, our results have $70 \sim 85\%$ of the value in the Stefan-Boltzmann limit. This result indicates that we cannot describe the 2-color QGP by the ideal gas model around $T/T_c \leq 2$.

For the scaling property, we also compare the result of the rescaled trace anomaly with the results in pure SU($N_c \geq 3$) gauge theories. Our result shows the different behavior from that in pure SU($N_c \geq 3$) gauge theories: the curved behavior around the critical temperature T_c, and the linear behavior in $(T_c/T)^2 \leq 0.6$. It is considered that the discrepancy comes from the difference of the order of the phase transition between pure SU(2) and pure SU($N_c \geq 3$) gauge theories.

One of the motivations of this study is the preparation for measuring the ratio of the shear viscosity and the entropy density η/s. The large-N_c analysis based on the AdS/CFT correspondence indicates that a lower bound is $\eta/s = 1/(4\pi)$ in pure SU(N_c) gauge theory. However, the correction terms of $1/N_c$ have not been determined yet. By using the results of pure SU(2) gauge theory, it is expected to provide information to determine the correction terms and lead to study properties of the vacuum of pure SU(N_c) gauge theory.

After measuring the thermodynamic quantities of pure SU(2) gauge theory as a function of temperature, we can construct the effective Polyakov loop potential used in an effective model for 2-color QCD such as the Polyakov-loop-extended Nambu–Jona-Lasinio (PNJL) model [2, 81–85]. By using this, it is possible to analyze the physics of 2-color QCD in the finite quark chemical potential region. Moreover, it is feasible to carry out lattice calculations of 2-color QCD, since there is no sign problem. Therefore, comparing both lattice and effective model results, we can check the efficiency of the effective model, and results of an effective model for 3-color QCD in the finite quark chemical potential region may become more reliable.

Chapter 4

Summary

QCD is the theory describing the dynamics of quarks and gluons, and the QCD states depend on temperature and the quark chemical potential. In the low temperature and the low quark chemical potential region, quarks are confined in hadrons. At high temperature, there is QGP where quarks and gluons behave almost as free particles, while quarks are in the color superconductor phase at the high quark chemical potential. The first-principle method to investigate these QCD states is LQCD. However, it is too difficult to perform LQCD calculations in the finite quark chemical potential region.

In this thesis, we adopt two approaches to investigate QCD properties in the finite quark chemical potential region: one is $\mathbb{Z}_3$-QCD, and the other is 2-color QCD.

$\mathbb{Z}_3$-QCD is the QCD-like model with exact $\mathbb{Z}_3$ symmetry, and agrees with the ordinary QCD in the zero temperature limit. In addition, the numerical result of the spin model indicates that the sign problem becomes milder by introducing exact $\mathbb{Z}_3$ symmetry to the model.

For further discussions, we performed the numerical simulations with the EPL model as an effective model of LQCD. Here, we used the phase quenched reweighting method to avoid the sign problem. Our results indicate that the region where the sign problem is serious becomes narrower via exact $\mathbb{Z}_3$ symmetry. We also proposed the improved reweighting method with the contribution of the imaginary part of the lattice action. The results with this method show that we can suppress the enlargement of the statistical errors coming from the reweighting method. Therefore, it is expected that the improved reweighting method makes the sign problem much milder in the lattice simulation of $\mathbb{Z}_3$-QCD.

In the phase quenched reweighting method, the imaginary part of the lattice action is ignored. This reweighting method is equivalent to introducing the isospin quark chemical potential. Due to this, the pion condensation occurs in LQCD simulations, and the sign problem becomes more serious at the large quark chemical potential. In contrast, our improved reweighting method includes the contribution of the imaginary part of the action. Hence,

it is expected that we can avoid the pion condensation by using the improved method.

We also carried out the calculations corresponding to the zero temperature limit. The result shows that the $\mathbb{Z}_3$-symmetric EPL model is consistent with the ordinary EPL model and there is no early onset of the quark number density. However, the EPL models we used are constructed in the large quark mass limit, and we cannot treat the chiral dynamics in the models. Thus, the early onset of the quark number density may occur in the lattice calculation of $\mathbb{Z}_3$-QCD.

In 2-color QCD, the sign problem is absent, and it is possible to make numerical calculations with the finite quark chemical potential. Thus, we can check the validity of an effective model by comparing the model result with the lattice result. To construct the effective model, we should measure thermodynamic quantities of pure SU(2) gauge theory. The thermodynamic quantities are also important to know properties of both 2-color and 3-color QCD. To measure the thermodynamic quantities, we use the gradient flow method.

We determined the scale-setting function via the dimensionless energy density. Our scale-setting function is more precise and covers the wider region of the lattice coupling than in the previous work. For the thermodynamic quantities, our results with the one-loop representation are consistent with the previous works in the high temperature region. Our result also shows that the behavior of the trace anomaly is different from pure SU($N_c \geq 3$) gauge theory: the curved behavior in $(T_c/T)^2 \lesssim 0.6$, and the linear one in $(T_c/T)^2 \gtrsim 0.6$. This may come from the difference of the order of the phase transition.

By using our data in the continuum limit, we can construct an effective model of 2-color QCD. Thus, after constructing the effective model, it is possible to investigate the 2-color QCD states in the finite quark chemical potential region and check the efficiency of the model. Due to this, it is expected that the reliability of results of the effective 3-color QCD model at the finite quark chemical potential is improved. On the other hand, after obtaining the shear viscosity η of pure SU(2) gauge theory, we can calculate the ratio of η to the entropy density with our results, and provide a signal to the correction terms of the large-N_c analyses.

Acknowledgment

First of all, I owe my deepest gratitude to Prof. Masanobu Yahiro. He taught me how interesting hadron physics are. He also supported my research and gave me warm encouragement. Without his guidance and persistent help, this thesis would not have been possible.

I would like to express my gratitude to Prof. Emiko Hiyama. She gave me useful comments and advice for this thesis, and provided an opportunity to get a job.

I would like to thank to Prof. Hiroaki Kouno and Research Assistant Prof. Etsuko Itou. They gave me a lot of beneficial comments on my research. Through many discussions with them, I was able to obtain many knowledge of lattice QCD simulations and hadron physics. I would like to appreciate Associate Prof. Yoshifumi R. Shimizu, Assistant Prof. Takuma Matsumoto, and Assistant Prof. Kouji Kashiwa for valuable comments about both nuclear and hadron physics in discussions, seminars and lessons. I would like to give my heartfelt appreciation to all members of the nuclear theory group in Kyushu University for their helpful comments and encouragements.

For practical supports, I am particularly grateful to Mako Nagata, Mariko Komori, Mayumi Takaki, Yuki Yamaji, Megumi Ieda, Atsuko Sono, and all other office workers.

The numerical simulations for pure SU(2) gauge theory were performed on the CRAY XC40 at Yukawa Institute for Theoretical Physics (YITP), Kyoto University, and the SX-ACE at Research Center for Nuclear Physics (RCNP), Osaka University.

Finally, I would like to offer my special thanks to my family and all other people for supporting my life.

Appendix A

Other results

A.1 Topological charge at finer lattice

It is known that the topological charge has a large autocorrelation time in SU(N_c) gauge theory [86]. Thus, by using the topological charge, we can study the autocorrelation of our gauge configurations. This quantity for pure SU(N_c) gauge theory in Euclidean spacetime is derived by

$$Q = \frac{1}{32\pi^2}\int d^4x\ \epsilon_{\mu\nu\rho\sigma}\mathrm{tr}_c\left[G^a_{\mu\nu}(t,x)G^a_{\rho\sigma}(t,x)\right], \tag{A.1}$$

where $G_{\mu\nu}(t,x)$ is the field strength composed by the flowed gauge field, and $\epsilon_{\mu\nu\rho\sigma}$ denotes the Levi-Civita symbol in the 4 dimension. The topological charge becomes integer in the continuum theory. However, in the lattice gauge theory, this property does not occur due to the UV fluctuations. In Refs. [42, 87, 88], it is shown that the method based on the gradient flow suppresses the effect of the UV fluctuations and the topological charge on the lattice can have the almost integer value.

Figure A.1 shows the result of Q for 600 configurations at $\beta = 2.85$, where the lattice spacing at $\beta = 2.85$ is the smallest in our simulations and the topological freezing may occur. For measuring the topological charge, we fix the flow time at $t/a^2 = 32$ to smear the link variable in the same range as $N_s/2$. It is seen that the value of Q is almost integer for each configuration and changes frequently for almost each configuration. Therefore, we can ignore the autocorrelation of our data.

A.2 Several reference values in t_0-scale

In Sec. 3.3, we obtain the scale-setting function which is valid in $2.420 \leq \beta \leq 2.850$. This function is suitable to investigate the thermodynamics in $T_c \lesssim T \lesssim 2T_c$. If we use the other reference value $A \equiv t^2\langle E(t)\rangle|_{t=t_0}$, we can also get the scale-setting function which is valid in the other range of β. Thus, we investigate the scale-setting function for the other reference value A.

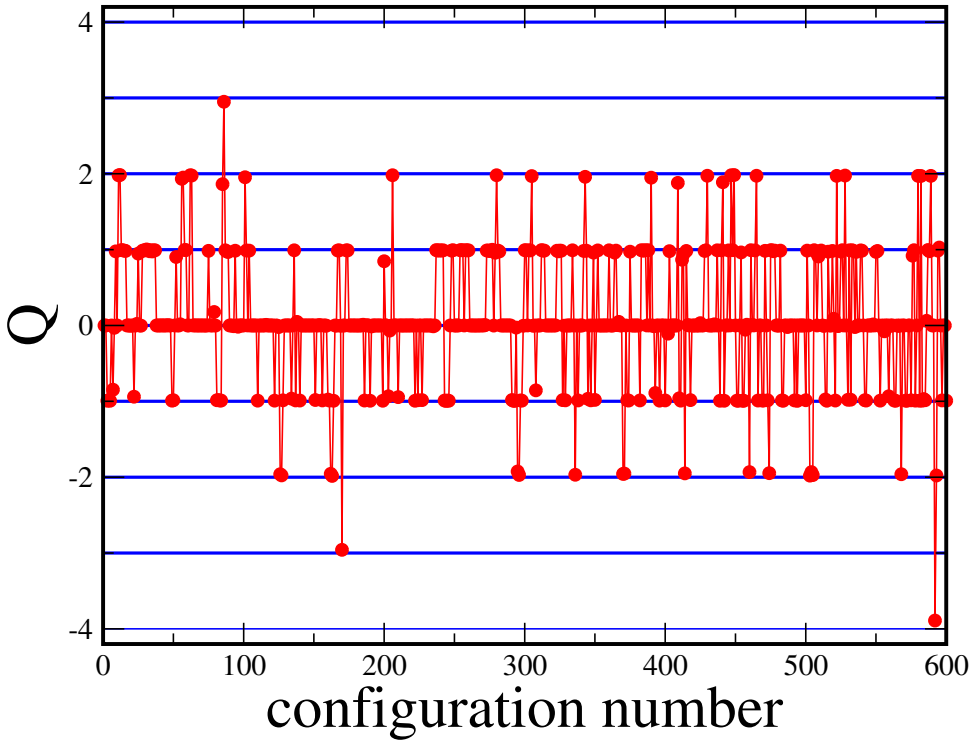

Figure A.1: Topological charge for 600 configurations at $\beta = 2.85$. We take 100 sweep separation between each configuration.

In Tab. A.1, the results of t_0/a^2 for other A are shown. The data in $\beta = 2.400$ for $A = 0.12$ is larger than 1, so we can use it to determine the scale-setting function. On the other hand, the data in both $\beta = 2.400$ and 2.420 for $A = 0.08$ and 0.09 are smaller than 1, and we need to ignore them to avoid the lattice discretization effect.

Table A.1: Results of t_0/a^2 for several A.

	t_0/a^2			
β	$A = 0.08$	$A = 0.09$	$A = 0.10$	$A = 0.12$
2.400	0.7264(9)	0.8400(12)	0.9549(5)	1.171(23)
2.420	0.8202(11)	0.9529(14)	1.083(2)	1.336(2)
2.500	1.372(2)	1.609(2)	1.839(3)	2.279(4)
2.600	2.612(7)	3.075(8)	3.522(10)	4.370(14)
2.700	4.881(25)	5.770(33)	6.628(36)	8.247(54)
2.800	8.780(74)	10.40(10)	11.96(12)	14.92(17)
2.850	12.25(10)	14.63(14)	16.95(17)	21.43(25)

Table A.2 shows the ratio of the lattice spacing a for each β to a_0 for $\beta = 2.600$, to study the A-dependence of the ratio a/a_0. The results for each A at the same β do not change much, so that the relation between β and a is almost independent of the selection of A.

Table A.2: Ratios of the lattice spacings a/a_0 for several A, where a_0 is the lattice spacing at $\beta = 2.600$.

	a/a_0			
β	$A = 0.08$	$A = 0.09$	$A = 0.10$	$A = 0.12$
2.400	1.896(3)	1.913(3)	1.921(3)	1,932(4)
2.420	1.784(3)	1.797(3)	1.803(3)	1.809(3)
2.500	1.380(2)	1.383(2)	1.384(2)	1.385(3)
2.600	1.000(2)	1.000(2)	1.000(2)	1.000(2)
2.700	0.7315(21)	0.7301(23)	0.7290(22)	0.7279(27)
2.800	0.5454(24)	0.5438(26)	0.5427(28)	0.5412(31)
2.850	0.4617(20)	0.4586(22)	0.4558(24)	0.4516(18)

By using the values for each A listed in Tab. A.2, we can obtain the scale-setting function with

$$\log(t_0/a^2) = \alpha_0 + \alpha_1(\beta - 2.600) + \alpha_2(\beta - 2.600)^2, \tag{A.2}$$

where α_i $(i = 0, 1, 2)$ are the fitting coefficients. Table A.3 shows the obtained coefficients and the fit range for several A. The coefficient α_0 is related to the value $\log(t_0/a^2)$ at $\beta = 2.600$ and depends on the selection of A. However, this dependence is not a problem since this term vanished when computing the ratio a/a_0. For both the coefficients α_1 and α_2, the results are almost independent of the selection of A. This result indicate that we can construct the scale-setting function which is available in the wider region of β by connecting the functions for several reference values A.

Table A.3: Coefficients of the scale-setting functions for several A.

A	α_0	α_1	α_2	fit range
0.08	0.9590(22)	6.343(16)	-0.8548(1360)	[2.500,2.850]
0.09	1.122(2)	6.382(18)	-0.8271(1493)	[2.500,2.850]
0.10	1.258(2)	6.409(14)	-0.7411(851)	[2.420,2.850]
0.12	1.474(2)	6.439(15)	-0.7501(846)	[2.400,2.850]

Bibliography

[1] S. Bethke, *Experimental tests of asymptotic freedom*, *Prog. Part. Nucl. Phys.* **58** (2007) 351 [hep-ex/0606035].

[2] K. Fukushima and T. Hatsuda, *The phase diagram of dense QCD*, *Rept. Prog. Phys.* **74** (2011) 014001 [1005.4814].

[3] A. M. Ferrenberg and R. H. Swendsen, *New Monte Carlo Technique for Studying Phase Transitions*, *Phys. Rev. Lett.* **61** (1988) 2635.

[4] C. R. Allton, S. Ejiri, S. J. Hands, O. Kaczmarek, F. Karsch, E. Laermann et al., *The QCD thermal phase transition in the presence of a small chemical potential*, *Phys. Rev.* **D66** (2002) 074507 [hep-lat/0204010].

[5] WHOT-QCD collaboration, *Equation of State and Heavy-Quark Free Energy at Finite Temperature and Density in Two Flavor Lattice QCD with Wilson Quark Action*, *Phys. Rev.* **D82** (2010) 014508 [0909.2121].

[6] G. Aarts, L. Bongiovanni, E. Seiler, D. Sexty and I.-O. Stamatescu, *Controlling complex Langevin dynamics at finite density*, *Eur. Phys. J.* **A49** (2013) 89 [1303.6425].

[7] D. Sexty, *Simulating full QCD at nonzero density using the complex Langevin equation*, *Phys. Lett.* **B729** (2014) 108 [1307.7748].

[8] G. Aarts, E. Seiler, D. Sexty and I.-O. Stamatescu, *Simulating QCD at nonzero baryon density to all orders in the hopping parameter expansion*, *Phys. Rev.* **D90** (2014) 114505 [1408.3770].

[9] AuroraScience collaboration, *New approach to the sign problem in quantum field theories: High density QCD on a Lefschetz thimble*, *Phys. Rev.* **D86** (2012) 074506 [1205.3996].

[10] H. Fujii, D. Honda, M. Kato, Y. Kikukawa, S. Komatsu and T. Sano, *Hybrid Monte Carlo on Lefschetz thimbles - A study of the residual sign problem*, *JHEP* **10** (2013) 147 [1309.4371].

[11] Y. Sakai, H. Kouno, T. Sasaki and M. Yahiro, *The quarkyonic phase and the Z_{N_c} symmetry*, *Phys. Lett.* **B718** (2012) 130 [1204.0228].

[12] H. Kouno, Y. Sakai, T. Makiyama, K. Tokunaga, T. Sasaki and M. Yahiro, *Quark-gluon thermodynamics with the Z(N(c)) symmetry*, *J. Phys.* **G39** (2012) 085010.

[13] H. Kouno, T. Misumi, K. Kashiwa, T. Makiyama, T. Sasaki and M. Yahiro, *Differences and similarities between fundamental and adjoint matters in SU(N) gauge theories*, *Phys. Rev.* **D88** (2013) 016002 [1304.3274].

[14] H. Kouno, T. Makiyama, T. Sasaki, Y. Sakai and M. Yahiro, *Confinement and $\mathbb{Z}_3$ symmetry in three-flavor QCD*, *J. Phys.* **G40** (2013) 095003 [1301.4013].

[15] H. Kouno, K. Kashiwa, J. Takahashi, T. Misumi and M. Yahiro, *Understanding QCD at high density from a Z_3-symmetric QCD-like theory*, *Phys. Rev.* **D93** (2016) 056009 [1504.07585].

[16] T. Iritani, E. Itou and T. Misumi, *Lattice study on QCD-like theory with exact center symmetry*, *JHEP* **11** (2015) 159 [1508.07132].

[17] T. Hirakida, H. Kouno, J. Takahashi and M. Yahiro, *Interplay between sign problem and Z_3 symmetry in three-dimensional Potts models*, *Phys. Rev.* **D94** (2016) 014011 [1604.02977].

[18] A. Nakamura, *Behavior of quarks and gluons at finite temperature and density in su (2) qcd*, *Phys. Lett.* **B149** (1984) 391.

[19] J. B. Kogut, M. A. Stephanov and D. Toublan, *On two color QCD with baryon chemical potential*, *Phys. Lett.* **B464** (1999) 183 [hep-ph/9906346].

[20] J. B. Kogut, D. K. Sinclair, S. J. Hands and S. E. Morrison, *Two color QCD at nonzero quark number density*, *Phys. Rev.* **D64** (2001) 094505 [hep-lat/0105026].

[21] S. Muroya, A. Nakamura and C. Nonaka, *Behavior of hadrons at finite density: Lattice study of color SU(2) QCD*, *Phys. Lett.* **B551** (2003) 305 [hep-lat/0211010].

[22] S. Hands, P. Sitch and J.-I. Skullerud, *Hadron Spectrum in a Two-Colour Baryon-Rich Medium*, *Phys. Lett.* **B662** (2008) 405 [0710.1966].

[23] S. Hands, S. Cotter, P. Giudice and J.-I. Skullerud, *The Phase Diagram of Two Color QCD*, 1210.6559.

[24] S. Cotter, J.-I. Skullerud, P. Giudice, S. Hands, S. Kim and D. Mehta, *Phase structure of QC2D at high temperature and density*, *PoS* **LATTICE2012** (2012) 091 [1210.6757].

[25] P. Cea, L. Cosmai, M. D'Elia and A. Papa, *Analytic continuation from imaginary to real chemical potential in two-color QCD*, *JHEP* **02** (2007) 066 [hep-lat/0612018].

[26] P. Cea, L. Cosmai, M. D'Elia and A. Papa, *The Critical line from imaginary to real baryonic chemical potentials in two-color QCD*, *Phys. Rev.* **D77** (2008) 051501 [0712.3755].

[27] T. Makiyama, Y. Sakai, T. Saito, M. Ishii, J. Takahashi, K. Kashiwa et al., *Phase structure of two-color QCD at real and imaginary chemical potentials; lattice simulations and model analyses*, *Phys. Rev.* **D93** (2016) 014505 [1502.06191].

[28] V. V. Braguta, E. M. Ilgenfritz, A. Yu. Kotov, A. V. Molochkov and A. A. Nikolaev, *Study of the phase diagram of dense two-color QCD within lattice simulation*, *Phys. Rev.* **D94** (2016) 114510 [1605.04090].

[29] K. Iida, E. Itou and T.-G. Lee, *Two-colour QCD phases and the topology at low temperature and high density*, 1910.07872.

[30] T. Brauner, K. Fukushima and Y. Hidaka, *Two-color quark matter: U(1)(A) restoration, superfluidity, and quarkyonic phase*, *Phys. Rev.* **D80** (2009) 074035 [0907.4905].

[31] K. Kashiwa, T. Sasaki, H. Kouno and M. Yahiro, *Two-color QCD at imaginary chemical potential and its impact on real chemical potential*, *Phys. Rev.* **D87** (2013) 016015 [1208.2283].

[32] J. Engels, J. Fingberg, F. Karsch, D. Miller and M. Weber, *Nonperturbative thermodynamics of SU(N) gauge theories*, *Phys. Lett.* **B252** (1990) 625.

[33] L. Giusti and M. Pepe, *Equation of state of the SU(3) YangMills theory: A precise determination from a moving frame*, *Phys. Lett.* **B769** (2017) 385 [1612.00265].

[34] J. O. Andersen, M. Strickland and N. Su, *Three-loop HTL gluon thermodynamics at intermediate coupling*, *JHEP* **08** (2010) 113 [1005.1603].

[35] A. Andronic, *An overview of the experimental study of quark-gluon matter in high-energy nucleus-nucleus collisions*, *Int. J. Mod. Phys.* **A29** (2014) 1430047 [1407.5003].

[36] D. T. Son and A. O. Starinets, *Viscosity, Black Holes, and Quantum Field Theory*, *Ann. Rev. Nucl. Part. Sci.* **57** (2007) 95 [0704.0240].

[37] A. Nakamura and S. Sakai, *Transport coefficients of gluon plasma*, *Phys. Rev. Lett.* **94** (2005) 072305 [hep-lat/0406009].

[38] H. B. Meyer, *A Calculation of the shear viscosity in SU(3) gluodynamics*, *Phys. Rev.* **D76** (2007) 101701 [0704.1801].

[39] S. Borsnyi, Z. Fodor, M. Giordano, S. D. Katz, A. Pasztor, C. Ratti et al., *High statistics lattice study of stress tensor correlators in pure $SU(3)$ gauge theory*, *Phys. Rev.* **D98** (2018) 014512 [1802.07718].

[40] N. Yu. Astrakhantsev, V. V. Braguta and A. Yu. Kotov, *Temperature dependence of the bulk viscosity within lattice simulation of $SU(3)$ gluodynamics*, *Phys. Rev.* **D98** (2018) 054515 [1804.02382].

[41] H. Suzuki, *Energymomentum tensor from the YangMills gradient flow*, *PTEP* **2013** (2013) 083B03 [1304.0533].

[42] M. Luscher, *Properties and uses of the Wilson flow in lattice QCD*, *JHEP* **08** (2010) 071 [1006.4518].

[43] M. Luscher and P. Weisz, *Perturbative analysis of the gradient flow in non-abelian gauge theories*, *JHEP* **02** (2011) 051 [1101.0963].

[44] FlowQCD collaboration, *Thermodynamics of SU(3) gauge theory from gradient flow on the lattice*, *Phys. Rev.* **D90** (2014) 011501 [1312.7492].

[45] Y. Taniguchi, S. Ejiri, R. Iwami, K. Kanaya, M. Kitazawa, H. Suzuki et al., *Exploring N_f = 2+1 QCD thermodynamics from the gradient flow*, *Phys. Rev.* **D96** (2017) 014509 [1609.01417].

[46] J. Greensite and K. Langfeld, *Effective Polyakov line action from the relative weights method*, *Phys. Rev.* **D87** (2013) 094501 [1301.4977].

[47] J. Engels, J. Fingberg and D. E. Miller, *Phenomenological renormalization and scaling behavior of SU(2) lattice gauge theory*, *Nucl. Phys.* **B387** (1992) 501.

[48] M. Panero, *Thermodynamics of the QCD plasma and the large-N limit*, *Phys. Rev. Lett.* **103** (2009) 232001 [0907.3719].

[49] M. Caselle, A. Nada and M. Panero, *Hagedorn spectrum and thermodynamics of SU(2) and SU(3) Yang-Mills theories*, *JHEP* **07** (2015) 143 [1505.01106].

[50] J. Greensite and K. Langfeld, *Finding the effective Polyakov line action for SU(3) gauge theories at finite chemical potential*, *Phys. Rev.* **D90** (2014) 014507 [1403.5844].

[51] J. Greensite, *Comparison of complex Langevin and mean field methods applied to effective Polyakov line models*, *Phys. Rev.* **D90** (2014) 114507 [1406.4558].

[52] M. Fromm, J. Langelage, S. Lottini and O. Philipsen, *The QCD deconfinement transition for heavy quarks and all baryon chemical potentials*, *JHEP* **01** (2012) 042 [1111.4953].

[53] G. Aarts and F. A. James, *Complex Langevin dynamics in the SU(3) spin model at nonzero chemical potential revisited*, *JHEP* **01** (2012) 118 [1112.4655].

[54] T. A. DeGrand and C. E. DeTar, *Phase Structure of QCD at High Temperature With Massive Quarks and Finite Quark Density: A Z(3) Paradigm*, *Nucl. Phys.* **B225** (1983) 590.

[55] I. O. Stamatescu, *A Note on the Lattice Fermionic Determinant*, *Phys. Rev.* **D25** (1982) 1130.

[56] T. Rindlisbacher and P. de Forcrand, *Two-flavor lattice QCD with a finite density of heavy quarks: heavy-dense limit and "particle-hole" symmetry*, *JHEP* **02** (2016) 051 [1509.00087].

[57] N. Garron and K. Langfeld, *Anatomy of the sign-problem in heavy-dense QCD*, *Eur. Phys. J.* **C76** (2016) 569 [1605.02709].

[58] A. M. Ferrenberg and R. H. Swendsen, *New monte carlo technique for studying phase transitions*, *Phys. Rev. Lett.* **61** (1988) 2635.

[59] S. Ejiri, *Existence of the critical point in finite density lattice QCD*, *Phys. Rev.* **D77** (2008) 014508 [0706.3549].

[60] T. D. . Cohen, *Functional integrals for QCD at nonzero chemical potential and zero density*, *Phys. Rev. Lett.* **91** (2003) 222001 [hep-ph/0307089].

[61] I. M. Barbour and A. J. Bell, *Complex zeros of the partition function for lattice QCD*, *Nucl. Phys.* **B372** (1992) 385.

[62] I. M. Barbour, S. E. Morrison, E. G. Klepfish, J. B. Kogut and M.-P. Lombardo, *The Critical points of strongly coupled lattice QCD at nonzero chemical potential*, *Phys. Rev.* **D56** (1997) 7063 [hep-lat/9705038].

[63] I. M. Barbour, S. E. Morrison, E. G. Klepfish, J. B. Kogut and M.-P. Lombardo, *Results on finite density QCD*, *Nucl. Phys. Proc. Suppl.* **60A** (1998) 220 [hep-lat/9705042].

[64] I. Barbour, S. Hands, J. B. Kogut, M.-P. Lombardo and S. Morrison, *Chiral symmetry restoration and realization of the Goldstone mechanism in the U(1) Gross-Neveu model at nonzero chemical potential*, *Nucl. Phys.* **B557** (1999) 327 [hep-lat/9902033].

[65] R. V. Harlander and T. Neumann, *The perturbative QCD gradient flow to three loops*, *JHEP* **06** (2016) 161 [1606.03756].

[66] T. van Ritbergen, J. A. M. Vermaseren and S. A. Larin, *The Four loop beta function in quantum chromodynamics*, *Phys. Lett.* **B400** (1997) 379 [hep-ph/9701390].

[67] R. Sommer, *A New way to set the energy scale in lattice gauge theories and its applications to the static force and alpha-s in SU(2) Yang-Mills theory*, *Nucl. Phys.* **B411** (1994) 839 [hep-lat/9310022].

[68] P. Giudice and S. Piemonte, *Improved thermodynamics of SU(2) gauge theory*, *Eur. Phys. J.* **C77** (2017) 821 [1708.01216].

[69] M. Luscher, S. Sint, R. Sommer and P. Weisz, *Chiral symmetry and O(a) improvement in lattice QCD*, *Nucl. Phys.* **B478** (1996) 365 [hep-lat/9605038].

[70] A. Ramos and S. Sint, *Symanzik improvement of the gradient flow in lattice gauge theories*, *Eur. Phys. J.* **C76** (2016) 15 [1508.05552].

[71] ALPHA collaboration, *Universality and the approach to the continuum limit in lattice gauge theory*, *Nucl. Phys.* **B437** (1995) 447 [hep-lat/9411017].

[72] S. Necco and R. Sommer, *The N(f) = 0 heavy quark potential from short to intermediate distances*, *Nucl. Phys.* **B622** (2002) 328 [hep-lat/0108008].

[73] J. Fingberg, U. M. Heller and F. Karsch, *Scaling and asymptotic scaling in the SU(2) gauge theory*, *Nucl. Phys.* **B392** (1993) 493 [hep-lat/9208012].

[74] B. A. Berg and D. A. Clarke, *Deconfinement, gradient and cooling scales for pure SU(2) lattice gauge theory*, *Phys. Rev.* **D95** (2017) 094508 [1612.07347].

[75] A. M. Eller and G. D. Moore, *Gradient-flowed thermal correlators: how much flow is too much?*, *Phys. Rev.* **D97** (2018) 114507 [1802.04562].

[76] S. Borsanyi, G. Endrodi, Z. Fodor, S. D. Katz and K. K. Szabo, *Precision SU(3) lattice thermodynamics for a large temperature range*, *JHEP* **07** (2012) 056 [1204.6184].

[77] T. Iritani, M. Kitazawa, H. Suzuki and H. Takaura, *Thermodynamics in quenched QCD: energymomentum tensor with two-loop order coefficients in the gradient-flow formalism*, *PTEP* **2019** (2019) 023B02 [1812.06444].

[78] M. Kitazawa, T. Iritani, M. Asakawa, T. Hatsuda and H. Suzuki, *Equation of State for SU(3) Gauge Theory via the Energy-Momentum Tensor under Gradient Flow*, *Phys. Rev.* **D94** (2016) 114512 [1610.07810].

[79] G. Boyd, J. Engels, F. Karsch, E. Laermann, C. Legeland, M. Lutgemeier et al., *Thermodynamics of SU(3) lattice gauge theory*, *Nucl. Phys.* **B469** (1996) 419 [hep-lat/9602007].

[80] M. Caselle, A. Nada and M. Panero, *QCD thermodynamics from lattice calculations with nonequilibrium methods: The SU(3) equation of state*, *Phys. Rev.* **D98** (2018) 054513 [1801.03110].

[81] P. N. Meisinger and M. C. Ogilvie, *Chiral symmetry restoration and Z(N) symmetry*, *Phys. Lett.* **B379** (1996) 163 [hep-lat/9512011].

[82] A. Dumitru and R. D. Pisarski, *Two point functions for SU(3) Polyakov loops near T(c)*, *Phys. Rev.* **D66** (2002) 096003 [hep-ph/0204223].

[83] A. Dumitru, Y. Hatta, J. Lenaghan, K. Orginos and R. D. Pisarski, *Deconfining phase transition as a matrix model of renormalized Polyakov loops*, *Phys. Rev.* **D70** (2004) 034511 [hep-th/0311223].

[84] A. Dumitru, R. D. Pisarski and D. Zschiesche, *Dense quarks, and the fermion sign problem, in a SU(N) matrix model*, *Phys. Rev.* **D72** (2005) 065008 [hep-ph/0505256].

[85] K. Fukushima, *Chiral effective model with the Polyakov loop*, *Phys. Lett.* **B591** (2004) 277 [hep-ph/0310121].

[86] ALPHA collaboration, *Critical slowing down and error analysis in lattice QCD simulations*, *Nucl. Phys.* **B845** (2011) 93 [1009.5228].

[87] C. Alexandrou, A. Athenodorou and K. Jansen, *Topological charge using cooling and the gradient flow*, *Phys. Rev.* **D92** (2015) 125014 [1509.04259].

[88] C. Bonati and M. D'Elia, *Comparison of the gradient flow with cooling in $SU(3)$ pure gauge theory*, *Phys. Rev.* **D89** (2014) 105005 [1401.2441].